

MASS-TRANSPORT FABRICATION  
OF  
REFRACTIVE GALLIUM-PHOSPHIDE MICRO-OPTICS

FINAL PROGRESS REPORT

JAMES R. LEGER

TODD A. BALLEEN

FREDRIK NIKOLAJEFF

U.S. ARMY RESEARCH OFFICE  
GRANT NUMBER DA/DAAH04-95-1-0360

DEPARTMENT OF ELECTRICAL AND COMPUTER ENGINEERING  
UNIVERSITY OF MINNESOTA  
MINNEAPOLIS, MINNESOTA 55455

APPROVED FOR PUBLIC RELEASE;  
DISTRIBUTION UNLIMITED

THE VIEWS, OPINIONS, AND/OR FINDINGS CONTAINED IN THIS REPORT ARE  
THOSE OF THE AUTHORS AND SHOULD NOT BE CONSTRUED AS AN OFFICIAL  
DEPARTMENT OF THE ARMY POSITION, POLICY, OR DECISION, UNLESS SO  
DESIGNATED BY OTHER DOCUMENTATION

# REPORT DOCUMENTATION PAGE

Form Approved  
OMB NO. 0704-0188

Public Reporting burden for this collection of information is estimated to average 1 hour per response, including the time for reviewing instructions, searching existing data sources, gathering and maintaining the data needed, and completing and reviewing the collection of information. Send comment regarding this burden estimate or any other aspect of this collection of information, including suggestions for reducing this burden, to Washington Headquarters Services, Directorate for Information Operations and Reports, 1215 Jefferson Davis Highway, Suite 1204, Arlington, VA 22202-4302, and to the Office of Management and Budget, Paperwork Reduction Project (0704-0188), Washington, DC 20503.

1. AGENCY USE ONLY (Leave Blank)	2. REPORT DATE December 1999	3. REPORT TYPE AND DATES COVERED Final Report
4. TITLE AND SUBTITLE Mass-Transport Fabrication of Refractive Gallium-Phosphide Micro-Optics		5. FUNDING NUMBERS DAAH04-95-1-0360
6. AUTHOR(S) James R. Leger, Todd A. Ballen, Fredrik Nikolajeff		8. PERFORMING ORGANIZATION REPORT NUMBER
7. PERFORMING ORGANIZATION NAME(S) AND ADDRESS(ES) University of Minnesota-Minneapolis Minneapolis, MN 55455		10. SPONSORING / MONITORING AGENCY REPORT NUMBER  ARO 33941.4-PH
9. SPONSORING / MONITORING AGENCY NAME(S) AND ADDRESS(ES) U. S. Army Research Office P.O. Box 12211 Research Triangle Park, NC 27709-2211		

11. SUPPLEMENTARY NOTES  
The views, opinions and/or findings contained in this report are those of the author(s) and should not be construed as an official Department of the Army position, policy or decision, unless so designated by other documentation.

12 a. DISTRIBUTION / AVAILABILITY STATEMENT  Approved for public release; distribution unlimited.	12 b. DISTRIBUTION CODE
---	-------------------------

Gallium-phosphide (GaP) refractive micro-optical elements have been fabricated by mass-transport smoothing. An approximation to the desired optical surface (the pre-form) is fabricated in a GaP substrate using anisotropic etching techniques. The pre-form is then smoothed into the final surface by the mass-transport process, in which surface-energy minimization drives material diffusion at elevated temperature in a sealed ampoule. A favorable variation of smoothing with the spatial period of the surface-relief structure allows the quick smoothing of the sharp edges of the pre-form while preserving the overall shape of the optical element. Refractive GaP micro-optical elements are demonstrated using single- and multi-step pre-forms, including a Fresnel biprism and an off-axis aspheric collimating lens. New pre-form designs are also introduced which relax fabrication tolerances. A concave mirror is fabricated and used for spatial-mode control of a vertical-cavity surface-emitting laser (VCSEL). The effect of the spacing of a sapphire cover-wafer above the GaP during mass-transport is investigated to test theoretical predictions of the relationship between surface and vapor diffusion. The surface roughness of a replicated GaP microlens is reduced by mass-transport. An array of off-axis GaP lenses is fabricated and integrated with an array of VCSELs to eliminate distortion in an optical interconnect system.

14. SUBJECT TERMS		15. NUMBER OF PAGES	
		16. PRICE CODE	
17. SECURITY CLASSIFICATION OR REPORT UNCLASSIFIED	18. SECURITY CLASSIFICATION ON THIS PAGE UNCLASSIFIED	19. SECURITY CLASSIFICATION OF ABSTRACT UNCLASSIFIED	20. LIMITATION OF ABSTRACT  UL

## Table of Contents

---

Table of Contents.....	2
List of Figures.....	4
1. Introduction.....	6
2. Modeling and Design of Mass-Transport Process	
2.1 Computer Simulation.....	7
2.2 Pre-Form Types.....	8
2.2.1 Multi-Level Pre-Forms.....	8
2.2.2 Single-Etch Pre-Forms.....	17
2.2.3 Other Etching Methods.....	24
3. Experimental Methods	
3.1 Introduction.....	26
3.2 Mask Generation.....	27
3.3 Photolithography.....	27
3.4 Etching Methods.....	28
3.5 Ampoule Cleaning and Sealing.....	29
3.6 Mass-Transport.....	31
4. Experiments	
4.1 Overview.....	32
4.2 Fresnel Biprism.....	33
4.3 Off-Axis Lens.....	38
4.4 VCSEL Spatial-Mode Control.....	41
4.5 Vapor/Surface Diffusion.....	56
4.6 Surface Roughness Reduction.....	58
4.7 Effects of Pre-Form Etching Errors.....	63
4.8 Optical Interconnection.....	66
5. Conclusions.....	76

6. List of Publications.....	77
7. List of Scientific Personnel & Advanced Degrees Earned.....	78
8. Bibliography.....	78

## List of Figures

---

2.1. Simulated smoothing of a vertical step and square-wave grating.....	8
2.2. Multi-step pre-form.....	9
2.3. Equal-mass design method for multi-step pre-form.....	10
2.4. Binary optics fabrication of 8-level element using 3 masks .....	11
2.5. Transport simulation with decreased top step height.....	13
3.6. Transport simulation with trench in top step and optimized step widths; 16 levels.....	15
2.7. Design of pixel for 1-dimensional binary pre-form method.....	18
2.8. Design of 1-dimensional binary pre-form for convex lens .....	19
2.9. Trapezoidal one-dimensional pre-form method.....	20
2.10. Reduced height range (20 – 80% of etch depth) for larger features.....	21
2.11. Two-dimensional fill-factor modulation design using square pixels.....	22
2.12. Design using 2-D fill-factor modulation and reduced height range .....	22
2.13. Hybrid 2-D/1-D fill-factor modulation method .....	23
2.14. Radially-symmetric one-dimensional fill-factor modulation for convex lens.....	24
2.15. Segmented concentric ring pre-form.....	25
2.16. Combination multi-level and single-etch pre-form.....	26
3.1. Diagram of mass-transport ampoule.....	30
4.1. Surface profilometer data for GaP biprism pre-form before transport .....	34
4.2. Surface profilometer data for GaP biprism after transport.....	35
4.3. Scanning interferometric microscope data for GaP biprism after transport.....	35
4.4. Experimental set-up for testing beam-steering of GaP biprism beam.....	36
4.5. Far-field intensity data for He-Ne beam steered to three locations.....	37
4.6. Simulated smoothing of a binary pre-form to generate an off-axis GaP lens .....	38
4.7. Surface profile of GaP off-axis lens after transport.....	39
4.8. Far-field intensity data for GaP off-axis lens.....	41
4.9. Micromirror integrated with a VCSEL for spatial-mode discrimination .....	43
4.10. Profilometer measurement of the fabricated GaP concave micromirror .....	45

4.11. Profilometer trace through center of the GaP micromirror; spherical fit to data.....	46
4.12. Experimental arrangement to test the micromirror.....	47
4.13. Spectral data for a 15- $\mu\text{m}$ VCSEL without spatial filtering.....	48
4.14. Spectral data for a 15- $\mu\text{m}$ VCSEL with spatial filtering.....	49
4.15. L-I curve for a 10- $\mu\text{m}$ VCSEL with and without spatial filtering .....	50
4.16. Method for replicating a microoptical structure into GaAs.....	51
4.17. Profilometer measurement of a biprism cast in a thin polymer film .....	53
4.18. Profilometer measurement of biprism after transfer into GaAs .....	54
4.19. Profilometer trace through the center of a micromirror replicated in GaAs .....	55
4.20. Interferogram of replicated GaAs micromirror.....	55
4.21. Diagram of mass-transport with cover wafer above rough GaP substrate.....	56
4.22. Amplitude decay of GaP surface roughness with cover wafer.....	58
4.23. SEM image of GaP microlens before and after mass-transport.....	59
4.24. AFM image of GaP microlens before and after mass-transport.....	61
4.25. Deviation of surface from parabola during mass-transport.....	62
4.26. Preservation of surface figure during mass-transport.....	63
4.27. Calibration plot of effective fill-factor vs. mask fill-factor.....	65
4.28. Optical interconnect system exhibiting distortion.....	67
4.29. Optical interconnect system using off-axis GaP microlenses for distortion correction.....	68
4.30. System diagram showing three object field points; perpendicular beams.....	69
4.31. Distortion as a function of object height for system in Fig. 4.30.....	70
4.32. System diagram showing three object field points; beams steered.....	70
4.33. OPD calculation for steered beams (three object field points).....	71
4.34. Image of aperture array through imaging system; simulation of Fig. 28.....	73
4.35. Image of VCSEL array incorporating beam-steering microlenses.....	74

## 1. Introduction

Micro lens arrays and single microlenses have found application in a wide variety of areas, including optical data storage, photocopy machines, focal-plane arrays, optical communication systems, laser beam shaping, *etc.* The most significant advantage to using micro-optics in many applications is the reduced size and complexity of the optical system. Often a bulky multi-element optical system requiring sophisticated opto-mechanical hardware can be replaced by a small micro-optical element that forms part of an integrated module. In addition, micro-optics sometimes provides the only viable solution to a particular optical problem.

The continued development of microelectronic integrated-circuit fabrication techniques during the last two to three decades of the twentieth century has made possible the simultaneous fabrication of large numbers of high-quality micro-optical elements by use of a number of techniques. One of these techniques is mass-transport smoothing, which allows the fabrication of an arbitrary optical surface directly in a III-V semiconductor material.

An approximation to the desired optical surface (the pre-form) is made on the surface of a III-V semiconductor material using standard microelectronic fabrication techniques. Mass-transport (material diffusion at elevated temperature) then smoothes out the sharp edges of the pre-form (the high-spatial-frequency components) to create the desired optical surface while leaving the overall shape of the element intact. The self-limiting nature of the mass-transport process also enhances its applicability as a viable technology for large-scale fabrication. After the small features of the pre-form have smoothed out, the larger horizontal features associated with the desired optical surface require transport times that are orders of magnitude larger to decay by the same amount. This greatly reduces the chance of inadvertently heating the sample for too long and destroying the desired profile.

The objective of this project is to apply the mass-transport smoothing technique to the fabrication of complex micro-optical elements. Refractive gallium-phosphide (GaP) micro-optical elements are demonstrated using single- and multi-step pre-forms, including a Fresnel biprism and an off-axis aspheric collimating lens. New pre-form designs with relaxed fabrication tolerance are also introduced. A concave mirror is fabricated and used for spatial-mode control of a vertical-cavity surface-emitting laser (VCSEL). This concave mirror has also been

replicated into a GaAs substrate by a casting and dry-etch transfer process. The effect of the spacing of a sapphire cover-wafer above the gallium-phosphide substrate during mass-transport is investigated to test theoretical predictions of the relationship between surface and vapor diffusion. An array of off-axis lenses is fabricated and integrated with an array of VCSELs to eliminate distortion in an optical interconnect system.

## 2. Modeling and Design of the Mass-Transport Process

### 2.1 Computer Simulation

The time evolution of a one-dimensional surface profile  $z(x,t)$  due to mass-transport smoothing can be written as a Fourier series:

$$z(x,t) = \sum_{n=0}^{\infty} A_n \exp(-t/\tau_n) \sin\left(\frac{2n\pi x}{\Lambda}\right), \quad (2.1)$$

where  $\Lambda$  is the spatial period and  $\tau_n$  is the characteristic decay lifetime given by:

$$\tau_n = \frac{1}{\gamma} \left(\frac{\Lambda}{2n\pi}\right)^4 = \frac{\Lambda^4 kT}{16n^4 \pi^4 \alpha v N_0 D_s}. \quad (2.2)$$

in which  $\gamma$  is the mass-transport parameter used in the surface evolution equation:

$$\frac{\partial z}{\partial t} = -\gamma \frac{\partial^4 z}{\partial x^4}. \quad (2.3)$$

Numerical solution of Equation (2.1) is possible using Fast Fourier Transform (FFT) computational methods. Calculation of the spatial FFT of the initial profile is followed by multiplication by the decaying temporal exponential term contained in Equation (2.1). As can be seen from Equation (2.2), the characteristic decay lifetime  $\tau_n$  contains several material parameters which are usually difficult to measure for a particular experimental situation. Therefore, for modeling of the mass-transport process a particular decay lifetime is measured experimentally and scaled as necessary for changes in temperature, spatial period, *etc.* Finally, the inverse spatial FFT is calculated to determine the resulting profile after smoothing. A comparison metric (such as rms surface error between the desired and simulated surfaces) is then calculated for the smoothed profile. An optimization routine is used to modify the transport time and initial pre-form profile to minimize the comparison metric.

An example of the computer simulation of the mass-transport process is shown in Figure 2.1, which displays the surface profile  $z(x,t)$  for several transport times. Figure 2.1a shows the time evolution of a single step; the rapid decay of the high-spatial-frequency components causes the tilt of the vertical step face. Figure 2.1b shows the behavior of a square-wave grating structure; the decay of the high-spatial-frequency terms quickly results in a sinusoidal profile (with period equal to that of the initial square-wave) whose amplitude slowly decays according to Equation 2.1.

## 2.2 Pre-Form Types

The mass-transport process occurs as a result of material diffusion driven by surface-energy minimization. For a particular set of transport parameters (time, temperature, and

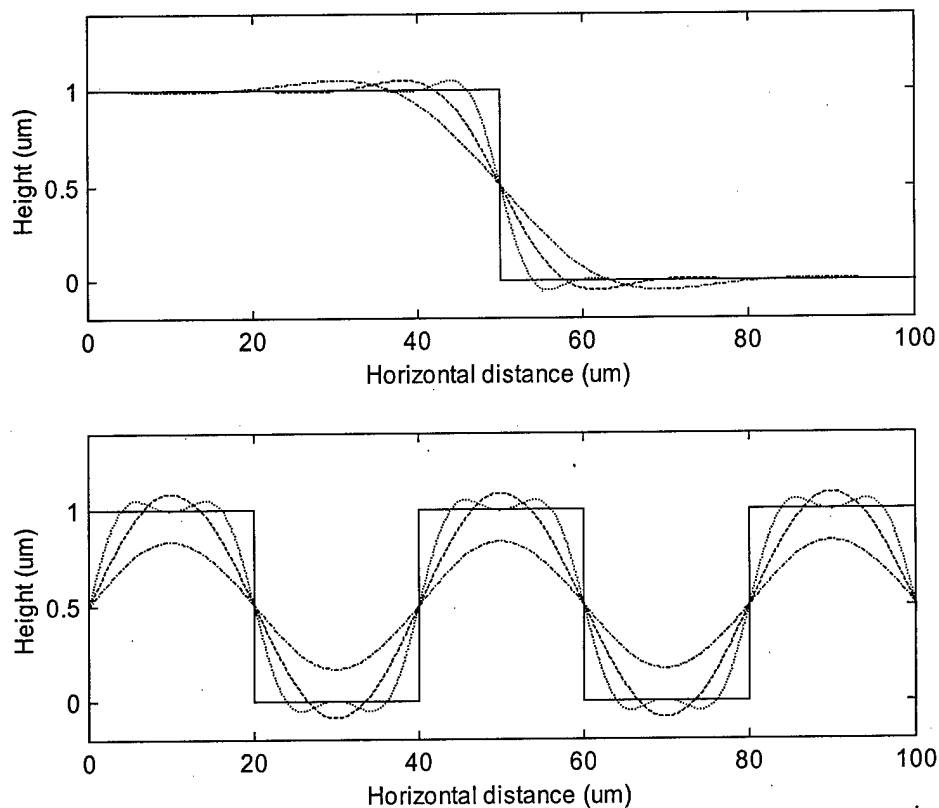


Figure 2.1. Simulated mass-transport smoothing of a vertical step (a) and square-wave grating (b); profile after zero (solid lines), 0.5 hours (dotted), 8 hours (dashed), and 64 hours (dot-dash).

phosphorous vapor concentration) the amplitude of a particular spatial wavelength will decay to a certain level deemed negligible in comparison to the desired surface (*e.g.* peak-to-valley amplitude difference  $< \lambda/4$ ). This implies that all horizontal features in the pre-form smaller than this critical size will also be smoothed out to a negligible level. Thus, it is unimportant exactly what shape the pre-form takes as long as the material in the pre-form is distributed in such a way that the desired surface is formed after diffusion. This is advantageous because it allows the pre-form to be made with whatever fabrication techniques are most convenient. The following sections describe several methods for designing the mass-transport pre-form; the process of fabricating the pre-form is discussed in Chapter 3.

### 2.2.1 Multi-Level Pre-Forms

The initial development of the mass-transport process in InP, then in GaP, for the fabrication of micro-optical elements used a series of concentric circular mesas as the pre-form [Liau, *et al.*, 1988; 1989]. Figure 2.2 shows a cross-section through the center of a structure designed to form a convex lens after mass-transport. As can be seen, the width of each step is 10

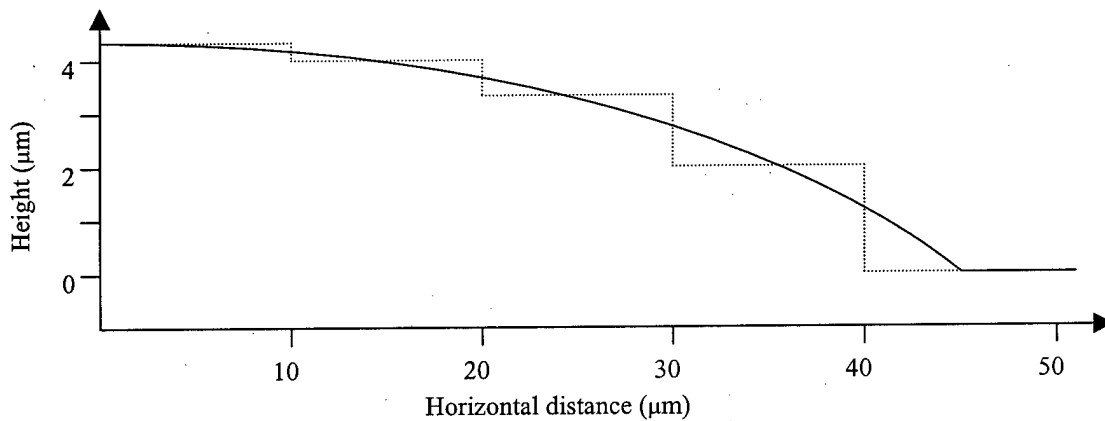


Figure 2.2. Multi-step pre-form before transport (dotted); after transport (solid).

$\mu\text{m}$ ; this is half of the largest spatial period which is completely smoothed during transport. The height of each step grows with increasing radius as the local surface slope becomes larger. This multi-step method was also used in the first demonstration of mass-transport fabrication of GaP micro-lenses using a sealed ampoule; the favorable conditions provided by the ampoule allowed

the increase of the step width to 30  $\mu\text{m}$ , reducing the number of steps needed to generate a lens of the same diameter [Swenson, *et al.*, 1995]. The multi-step method has the advantage of large feature sizes, *i.e.* the smallest defined feature for the pre-form shown in Figure 2.2 is a circle with diameter = 20  $\mu\text{m}$  (as seen if Figure 2.2 is rotated about its vertical axis). In the earliest demonstrations [Liau, *et al.*, 1988; 1989] the large horizontal size and relatively small vertical height of the multi-level steps allowed the definition of the pre-form by simple wet-etching techniques.

With the assumption that the slope changes slowly the pre-form can be designed using a simple “equal-mass” rule [Liau, *et al.*, 1988]. This method, shown schematically in Figure 2.3, assumes that mass is conserved during transport; therefore the mass (and hence the volume) above and below each step is equalized. The multi-step method has several disadvantages,

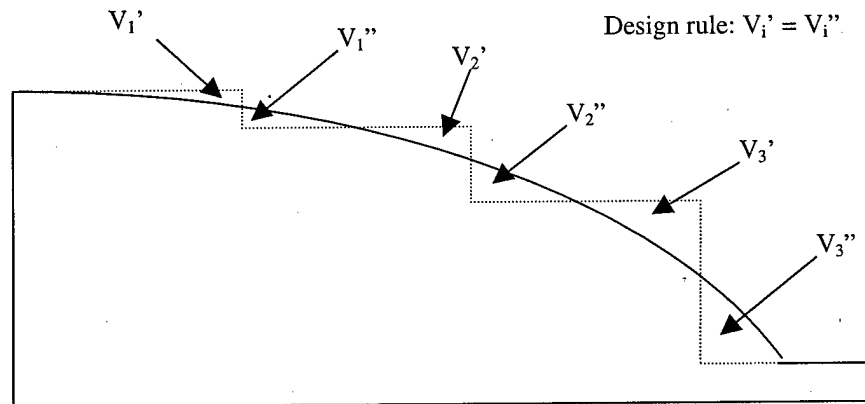


Figure 2.3. Equal-mass design method for multi-step pre-form;  
Before transport (dotted), after transport (solid).

however. As the step width is limited to ~20-30  $\mu\text{m}$  by the physical parameters of the transport process in GaP, a lens with a diameter of hundreds of microns requires many levels. As described in Chapter 3, each of these mesa levels requires a separate mask-and-etch step, and must be precisely aligned to preceding layers and etched with great depth accuracy. Errors in layer alignment or step height result in distortion of the surface after mass-transport which has a negative impact on the optical performance of the element [Liau, *et al.*, 1994d].

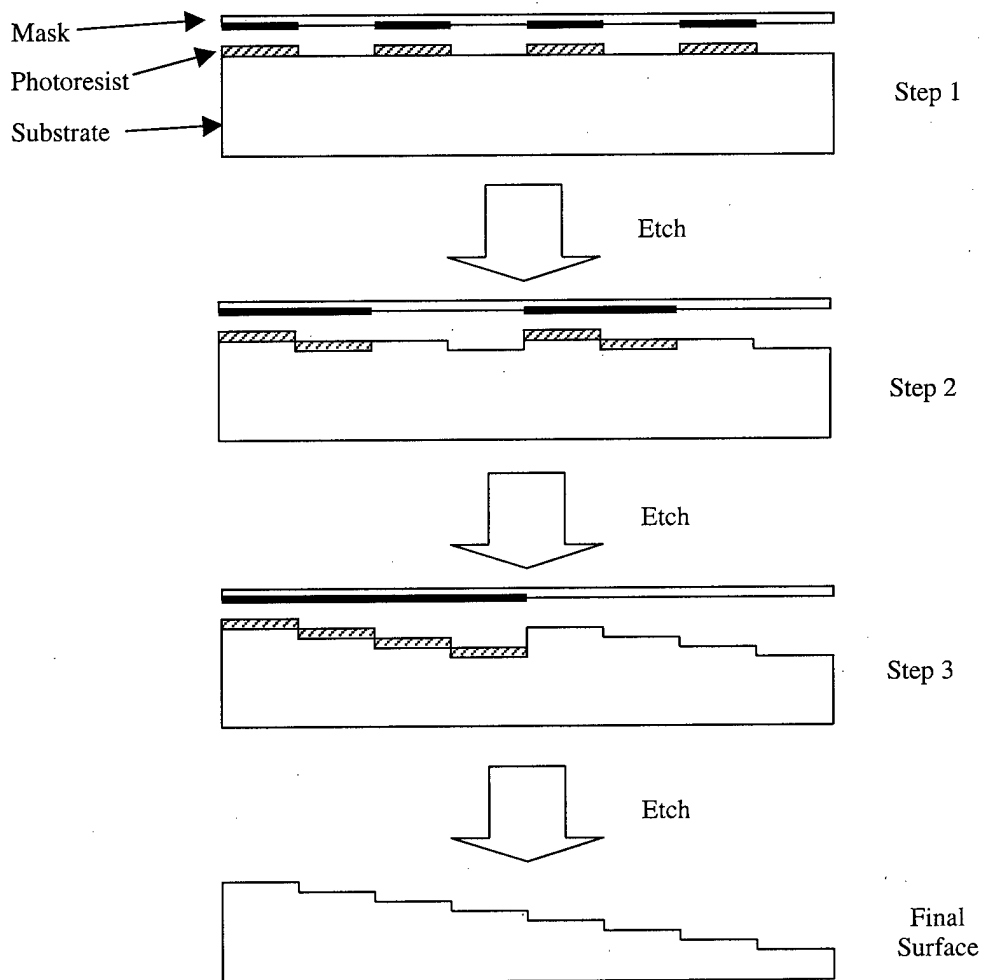


Figure 2.4. Binary optics fabrication of 8-level element using 3 masks; after [Swanson, 1989].

The number of separate fabrication steps to produce a multi-level pre-form can be reduced by using some of the techniques used to fabricate diffractive optical elements [Swanson, 1989]. The “binary optics” technique, as it has come to be known, is illustrated in Figure 2.4 for the case of an eight-level structure. (More detail about each of the steps shown in Figure 2.4 is contained in Chapter 3.) The first mask-and-etch step generates small features etched to one-seventh of the total height of the structure. The second and third fabrication steps pattern larger features and etch depths of two- and four-sevenths the height of the structure, respectively. Thus, eight levels (or seven steps) have been generated from three mask-and-etch steps. In general, it is possible to generate  $2^m$  levels with  $m$  mask-and-etch steps. While this technique was developed for the fabrication of diffractive optics (where a surface relief structure is used to define an optical phase function ranging from 0 to  $2\pi$ ) the “ $2^m$ ” method is suitable for the

generation of other multi-level structures. The primary restriction on a multi-level structure made with this technique, however, is that the depth of each level belongs to a small set of values. In the example shown in Figure 2.4, the depth of each level is an additive combination of the individual etch depths. Typically, each of the steps has the same height, and a particular etch depth  $d_i$  for one part of the fabrication sequence shown in Figure 2.4 is calculated as:

$$d_i = \left( \frac{i}{2^m - 1} \right) h \quad (2.4)$$

where  $m$  is the total number of masks,  $i$  is the current mask number ( $i = 1, 2, 3, \dots, m$ ), and  $h$  is the total height of the structure.

For a multi-level approximation to a convex lens using the “binary-optics” approach outlined above, a structure with steps of equal height and varying width results. In this case the change in step width controls the local slope, in contrast to the other multi-level method discussed previously, in which the step height controls the slope. While a variation in step width may be viewed as problematic when this multi-level structure undergoes mass-transport, it can work well under the proper circumstances. As discussed in the introduction to this section, all horizontal features smaller than a particular critical size decay to a negligible level for a particular set of mass-transport conditions. Thus, as long as the mass-transport parameters are chosen such that the largest horizontal step smooths out, the absolute size of all other steps is irrelevant. Therefore it is possible to reduce the number of fabrication steps needed to make the pre-form by taking advantage of the “ $2^m$  process”.

Complications in this method, however, arise at places where the slope is no longer moderate. Near the center of a convex lens the slope becomes small, resulting in large step widths. Likewise, the slope becomes large near the lens perimeter, resulting in small step widths. As mentioned above, if the transport parameters are chosen such that the largest step is smoothed, all of the other steps will be smoothed out as well. However, if the number of levels in the pre-form is too small, the top step can be quite large; this leads to prohibitively long transport times with additional complications. This problem can be solved by the addition of more mask steps which increases the number of levels and decreases the largest step width.

The  $2^m$  multi-level mass-transport fabrication of a 0.71 NA (numerical-aperture) aspheric GaP lens (design wavelength of 650 nm) was modeled with a computer simulation. The lens has a surface profile given by:

$$z = \frac{ch^2}{1 + \sqrt{1 - (1+k)c^2h^2}} + a_4h^4 + a_6h^6, \quad (2.5)$$

where  $z$  is the surface height at radial location  $h$ ,  $c$  is the vertex curvature (defined as 1/radius-of-curvature),  $k$  is the conic constant, and  $a_4$  and  $a_6$  are the 4th and 6th-order aspheric coefficients, respectively. For each simulation, a pre-form chosen using the "equal-mass" approach described above is smoothed via mass-transport in such a way as to minimize the rms error between the resulting surface and the desired optical surface. Discontinuities in the surface profile involve high-spatial-frequency components which are not preserved during mass-transport. These regions, such as the lens perimeter, are distorted during the transport process. To avoid the complications of these edge effects it is necessary to design the diameter of the lens to be larger than the useful aperture; in this way the distortions caused by edge effects at discontinuities remain outside of the useful optical surface.

The first simulation result to produce the surface profile given by Equation 2.5 is shown

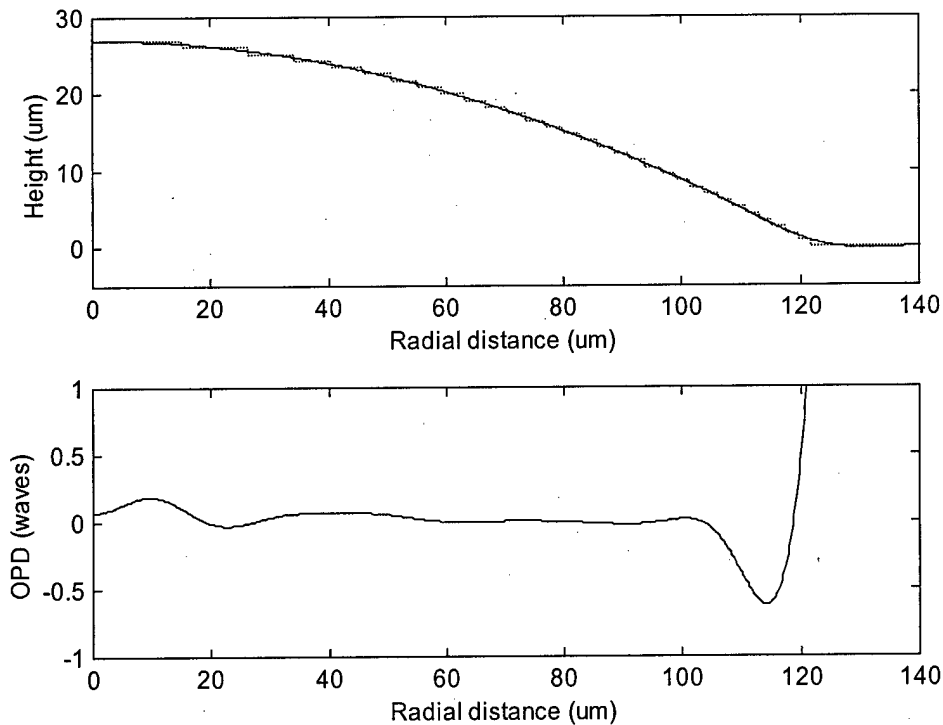


Figure 2.5. (a) Simulation before (dotted) and after transport (solid) with decreased top step height  
 (b) Optical path difference between simulated and design surfaces.

in Figure 2.5, in which five mask steps have been used to produce a 32-level multi-step pre-form. The optimum transport time (at 1100 °C) to minimize the rms optical path difference (OPD) across the useful part of the lens (0 – 108  $\mu\text{m}$ ) was found to be approximately 0.7 hours. (The transport times used in computations have been calibrated by adjusting the theoretical diffusion parameters to yield simulations that match experimental results.) The short transport time is the result of the large number of steps which causes even the widest step to be relatively small, and therefore to smooth out quickly. The lens half-diameter has been increased in the design by 15  $\mu\text{m}$  to move the edge distortion outside the lens aperture. Figure 2.5a shows the pre-form (dotted line) and the profile after transport (solid line), while Figure 2.5b plots the OPD across the surface; the rms OPD across the desired portion of the lens is less than  $\lambda/10$ . An additional etching step has been used to lower the top step to 92% of its original height; this reduction in height was chosen to minimize the rms OPD by reducing the height of the peak in the OPD (at a radial distance of  $\sim 10 \mu\text{m}$ ) in Figure 2.5b. While this modification improves the surface figure, it is still apparent that the surface distortion caused by the top two pre-form steps is still the largest contribution to the rms OPD.

In addition to reducing the height of the top step, the surface distortion near the lens center can be controlled by modifying the width of the top step. This can be accomplished by defining an offset or piston term, which is the difference between the height of the optical surface on the optical axis and the total height of the pre-form. This is possible because there is a net diffusion of material from the edge of the top step toward the center during the initial stages of mass-transport (as the high-spatial-frequency components decay). Therefore, the height of the final surface can be slightly larger than the height of the pre-form. By changing this offset the width of the top step can be modified to reduce the surface error near the center of the lens.

Another approach to minimize surface distortion caused by a wide top step is to increase the transport time so that the spatial period associated with the width of the top step is attenuated to a greater extent. Although this has the desired effect near the lens center, there is a net diffusion of material away from the lens profile at the perimeter. These edge effects are seen as a negative depression in the OPD curve near the perimeter of the lens; this depression moves further into the lens aperture as the transport time increases. These edge effects can be kept out of the used area of the lens by further increasing the design diameter of the lens.

The previous simulation (shown in Figure 2.5) has been modified to include an offset in the height of the design surface, as well as an increase in the lens diameter and transport time. In this case, a 32-level structure designed with a  $35\ \mu\text{m}$  increase in half-diameter, and with an offset of  $-10\%$  of the height of the top step, had a minimum rms OPD over the desired region after 11.34 hours of transport. The longer transport time more completely smoothes out the top step, though at the expense of further distortion near the lens perimeter. The rms OPD across the used lens aperture for this simulation is nearly the same as that of the previous example ( $\sim\lambda/10$ ). Additional improvement in the rms OPD is expected with a further increase of the lens diameter, although at this point the portion of the lens sacrificed to edge effects constitutes a considerable fraction of the total lens area.

In each of the above simulations using a  $2^m$  pre-form the large width of the top step in comparison with other steps caused problems. A relatively short transport time that smoothed the small steps at the perimeter of the lens while preserving the lens profile left a substantial

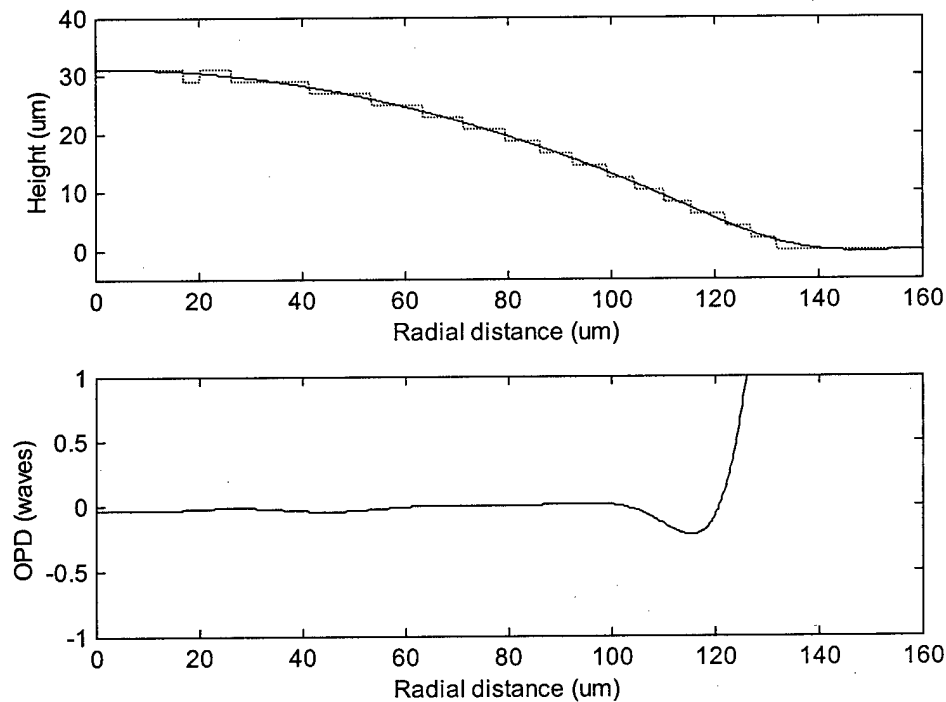


Figure 2.6. (a) Simulation before (dotted) and after transport (solid) with trench in top step and optimized step widths; 16 levels; (b) Optical path difference between simulated and design surfaces.

distortion at the lens center due to the incomplete smoothing of the top step (as seen in Figure 2.5). Increasing the transport time to completely smooth this large feature resulted in unwanted distortion of the lens edges, which could only be corrected by over-designing the lens with a larger diameter than needed. However, it is possible to alleviate these problems through a small modification of the pre-form profile that does not involve additional fabrication steps.

The top step smoothes so slowly because it is large and the fourth-power dependence of the mass-transport process (Equation 2.2) requires a much longer time for sufficient amplitude decay of this component. If, however, a trench is etched into the top step to divide it into several pieces, then the size of the largest horizontal feature is reduced and the transport time needed for effective smoothing is substantially decreased. Also, the widths of the other steps can be changed from the values chosen by the "equal-mass" rule to values that reduce the OPD in the vicinity of each step. An example of the power of the combination of these techniques is shown in Figure 2.6, in which a 16-level (four masks) pre-form has been designed; the optimum transport time after simulated smoothing is  $\sim 5.2$  hours. Figure 2.6a shows the pre-form (dotted line) and the profile after transport (solid line), while Figure 2.6b plots the OPD across the surface. For this simulation an offset of  $-3.5\%$  of the height of the top step was used, and the lens half-diameter was increased by  $25 \mu\text{m}$  to reduce distortion at the edges. The width of most of the steps has been altered from the value calculated using the "equal-mass" method. The width of each step was changed while observing the change of the OPD curve in the vicinity of the step; a minimum rms OPD was the optimization goal. The step widths were altered manually, but this process can be implemented as part of an automatic global optimization routine. A trench (width =  $3.0 \mu\text{m}$ ) centered at a position of  $18.5 \mu\text{m}$  has been used to divide the top step into smaller pieces. This trench does not increase the fabrication complexity, however, because it is etched as part of the same masking step that patterns the top step; in addition, the trench is relatively wide and can be easily defined. The combination of these improvements yields a much lower rms OPD of  $\sim \lambda/50$  across the design aperture.

If a slight increase in the rms OPD is acceptable, the techniques used in the previous example can be used to further reduce the number of fabrication steps. The previous simulation was repeated using an 8-level (3-mask) multi-level pre-form for an optimum transport time of 32 hours. For this simulation an offset of  $-8.75\%$  of the height of the top step was used, and the lens half-diameter was increased by  $25 \mu\text{m}$  to reduce distortion at the edges. All step-widths

have been altered from the values calculated using the “equal-mass” method. As in previous examples the increase in transport time is the result of the larger width of the top step. The increase in the height of the top step (and thus of the depth of the trench), however, results in a decrease of the width of the added trench to 1.5  $\mu\text{m}$ , centered at a position of 24.0  $\mu\text{m}$ . The rms OPD across the desired lens surface is  $\sim\lambda/40$ . The problem with this 8-level technique as compared to the previous 16-level is the six-fold increase in transport time. Suppression of the smoothing process by oxide contamination after a long transport time has been observed [Swenson, *et al.*, 1995] and may lead to incomplete smoothing of the pre-form. Furthermore, the aspect ratio of the trench in the top step is much larger for the 8-level design (4.0  $\mu\text{m}$  depth x 1.5  $\mu\text{m}$  width) than for the 16-level design (2  $\mu\text{m}$  depth x 3  $\mu\text{m}$  width). This may make the trench for the eight-level design too difficult to fabricate by some techniques. The addition of a single trench to the top step of a multi-level pre-form can be considered a specific example of a more general technique that uses many trenches to allow extensive modification of a surface generated from a multi-level pre-form. This approach is discussed in greater detail in Section 2.2.3.

### 2.2.2 Single-Etch Pre-Forms

To overcome the fabrication complexity associated with aligning and etching multiple layers in the one-mask-per-level method, a self-aligned single-etch technique was developed for pre-form fabrication [Liau, *et al.*, 1994a]. In this method, the desired optical surface is divided into a two-dimensional array of pixels whose lateral size is smaller than the largest spatial period that is removed during transport. This technique also uses an “equal-mass” technique; in this case the mass in each pixel is the same before and after transport. A diagram of the design methodology is shown in Figure 2.7 for a single pixel, where Figure 2.7a shows a cross-section of the pixel and Figure 2.7b is a top view; in both figures the shaded region is the un-etched section. The pre-form etch-depth  $H$  is larger than the final height (the sag) of the optical element, and, in particular, is larger than the height of the optical surface in the pixel  $H_i$ . This causes the fill factor (the ratio of the cross-sectional area of the remaining mass in the particular pixel to the total pixel area) of each pixel to be less than unity. Using the definitions of Figure 2.7, where  $P_x$  and  $P_y$  are the sizes of the pixel in the x and y direction, respectively, equalization of the volume (and thus the mass) in the pixel before and after mass-transport yields:

$$\left( H \cdot W_i \cdot P_y \right) = \left( H_i \cdot P_x \cdot P_y \right). \quad (2.6)$$

The pixel fill factor ( $W_i/P_x$ ) is therefore the ratio of the height of the desired optical surface in the pixel to the initial etch depth ( $H_i/H$ ). As shown in Figure 2.7b, the fill factor in the vertical (y) direction is held constant at unity, while the horizontal fill factor is allowed to vary; this results in long mesas that span the entire lens aperture. In the case of a typical convex lens, these mesas are widest (and in closest proximity to each other) near the center of the lens and become thinner near the edge of the lens, as shown in Figure 2.8.

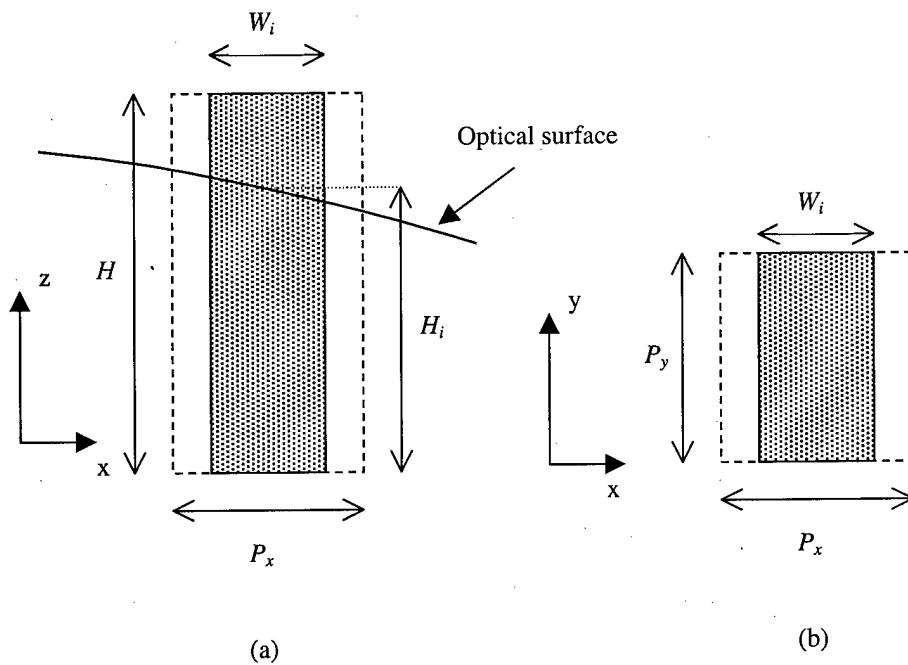


Figure 2.7. Design of pixel for 1-dimensional binary pre-form method: (a) Side view; (b) Top view.

Figure 2.8 shows how the mesa width changes with the design height of the optical surface for a convex lens. The square corners at the edges of the mesa (marking the interface between pixels) present a special fabrication challenge. These square corners become rounded as a result of diffraction effects in the photolithography process used to pattern the pre-form. This has a deleterious effect on the final surface, since a variation in the mass contained within a pixel in the pre-form results in a change in the final surface height in the pixel after transport. While it is possible to compensate for these diffraction effects to generate square corners using an electron-beam exposure system [Hagberg, *et al.*, 1992], this is often impractical for an optical exposure. It is possible, however, to minimize the negative effects of diffraction through a small change in the pre-form design.

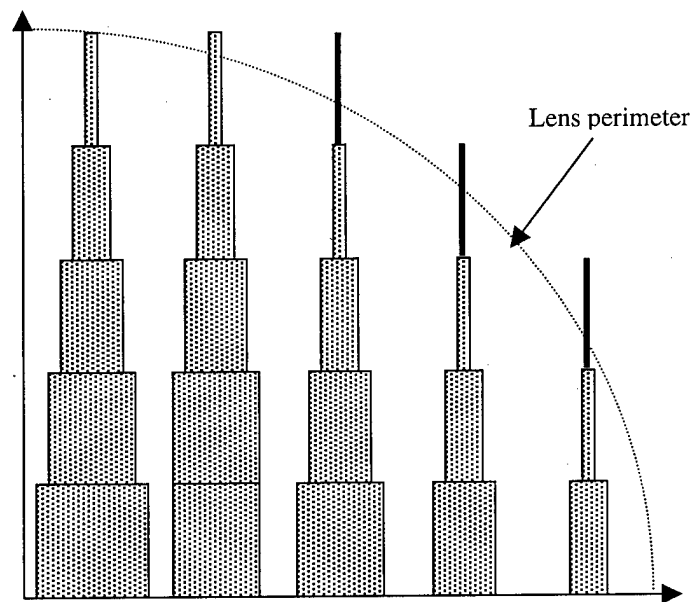


Figure 2.8. Design of 1-dimensional binary pre-form for convex lens (top view of one quadrant).

Assuming that diffusion during mass-transport smoothes out any features within a particular pixel, the final surface height of the pixel is unchanged provided that the mesa area within the pixel remains constant. Therefore, it is possible to use a trapezoidal mesa section in each pixel, rather than the rectangular one discussed above. Figure 2.9 shows a top-view of two adjacent pixels designed using this trapezoidal method. The height of each trapezoid remains  $P_y$ , thus preserving the unity  $y$ -axis fill-factor and the resulting long mesas of varying width. The widths of the top and bottom sides of each trapezoid are chosen to provide the necessary total

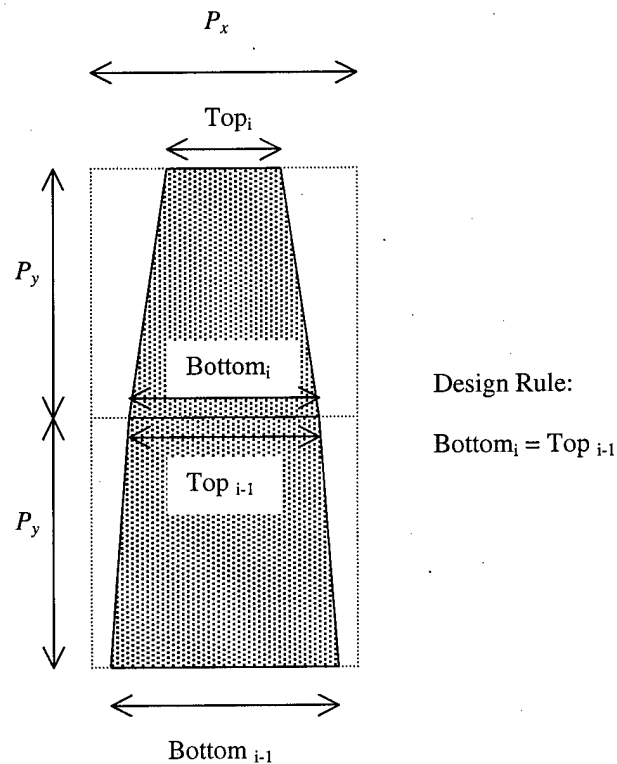


Figure 2.9. Trapezoidal one-dimensional pre-form method (top view)

area within the pixel. The only restriction is that the width of the base of a particular trapezoid must equal the width of the top of the trapezoid contained in the pixel immediately below the pixel under consideration. This generates long mesas of gradual width variation with sides that are nearly continuous curves. The diffraction effects in the photolithography process for this type of pre-form are less severe than those for the rectangular pixel pre-form method. The trapezoidal method therefore allows more accurate definition of the pre-form.

As mentioned above, both of these single-etch methods (the rectangular and trapezoidal one-dimensional fill-factor modulation) have the advantage of not requiring alignment to previous layers. This eliminates errors caused by mis-registration of layers, as well as reducing the effects of etch-depth errors. The difficulty with these single-etch techniques employing one-dimensional mesa width modulation to encode the surface height, however, lies in the need to generate high aspect-ratio structures (small horizontal and large vertical dimensions). As the sag of the optical element increases, the fill-factor of pixels near the perimeter of the element decreases, increasing the aspect-ratio (mesa height/width) of the mesas at these locations. Similarly, as the sag of the optical element approaches the size of the initial etch depth, the fill-

factor of pixels near the highest point of the element approach unity, increasing the aspect-ratio of the trenches between mesas.

This problem can be alleviated by reducing the dynamic range of the allowable final surface height. Instead of allowing the optical surface height in a pixel to range from zero to the etch depth, the height can be restricted to an intermediate range, such as 20 - 80% of the etch depth, as shown in Figure 2.10. The smallest horizontal feature is thus enlarged by sacrificing some of the sag of the lens available by etching to a particular depth. This can be seen by examining a typical case of a convex lens in which the pixel width  $P_x$  is 10 - 15  $\mu\text{m}$ . A pixel near the perimeter of such a pre-form (where the final surface height is close to minimum) has an area fill-factor of  $\sim 20\%$  for the 20 - 80% modulation design. This leads to a width fill-factor of  $\sim 20\%$ , since the  $y$ -axis fill-factor is unity, which in turn results in a minimum mesa width of 2 - 3  $\mu\text{m}$ . This minimum feature size is easier to fabricate than the minimum feature that results from allowing the fill-factor to come arbitrarily close to zero.

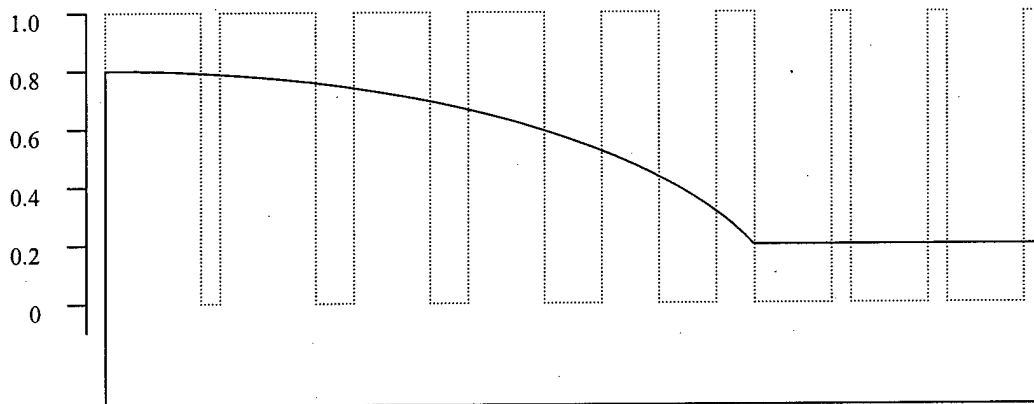


Figure 2.10. Reduced height range (20 - 80% of etch depth) for larger features (side view); before transport (dotted line) and after transport (solid line).

Using the 20 - 80% area-modulation method described in the previous paragraph, the size of the minimum feature can be further increased by removing the restriction that the  $y$ -axis fill-factor of each pixel remains unity. By allowing the fill-factor in both the  $x$ - and  $y$ -directions to vary, the mesa width increases, as shown in Figure 2.11. The width  $W_i$  of each mesa is given by:

$$W_i = P\sqrt{ff_i} \quad (2.7)$$

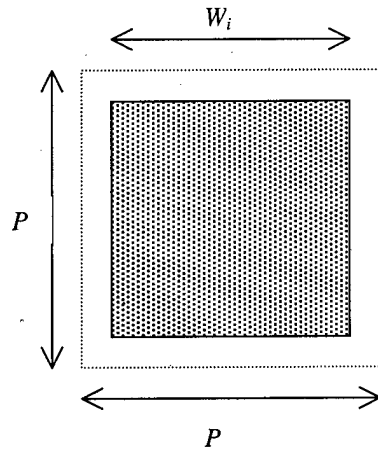


Figure 2.11. Two-dimensional fill-factor modulation design using square pixels (top view)

where  $P$  is the size of the pixel and  $ff_i$  is the area fill-factor of a particular pixel. A design for a convex lens using this two-dimensional fill-factor modulation method is shown in Figure 2.12.

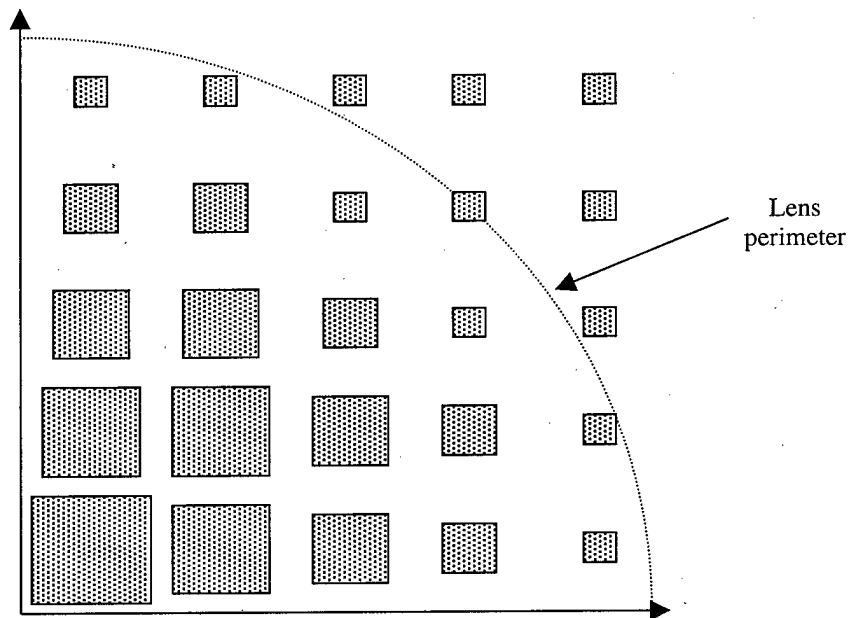


Figure 2.12. Design of convex lens using 2-D fill-factor modulation and reduced (20 – 80%) height range with square pixels (top view of one quadrant)

Using the example from the previous paragraph, a pre-form designed using the 20 – 80% modulation range with a pixel size of 10 - 15  $\mu\text{m}$  gives a minimum mesa width of  $\sim 4.5 - 6.7 \mu\text{m}$ . Such features are even easier to fabricate than those produced using the one-dimensional fill-factor modulation technique. A problem exists at the maximum end of the modulation range, however. A pixel designed to give the maximum 80% height has a mesa width fill-factor ( $W_i / P$ ) of  $\sim 0.89$ ; for a pixel size of 10 - 15  $\mu\text{m}$  this results in a mesa width of  $\sim 8.9 - 13.4 \mu\text{m}$ . The patterning of these structures is not the problem, but rather the fact that such mesas will be close to one another (for example near the optical axis of a convex lens, where the slope changes very slowly). In such places, the etched region (area between mesas) will have a minimum width of  $\sim 1.0 - 1.5 \mu\text{m}$ . Such a high-aspect-ratio trench will provide fabrication challenges similar to those met in fabricating a high-aspect-ratio mesa. Thus, the benefit gained in the two-dimensional fill-factor-modulation method by enlarging the minimum feature is offset by the reduction in space between mesas at the highest parts of the optical element.

It is, however, possible to combine the one- and two-dimensional fill-factor-modulation techniques by using each method in the region where it is most advantageous. An example of this is shown in Figure 2.13. Beginning at the center of the convex lens, one-dimensional

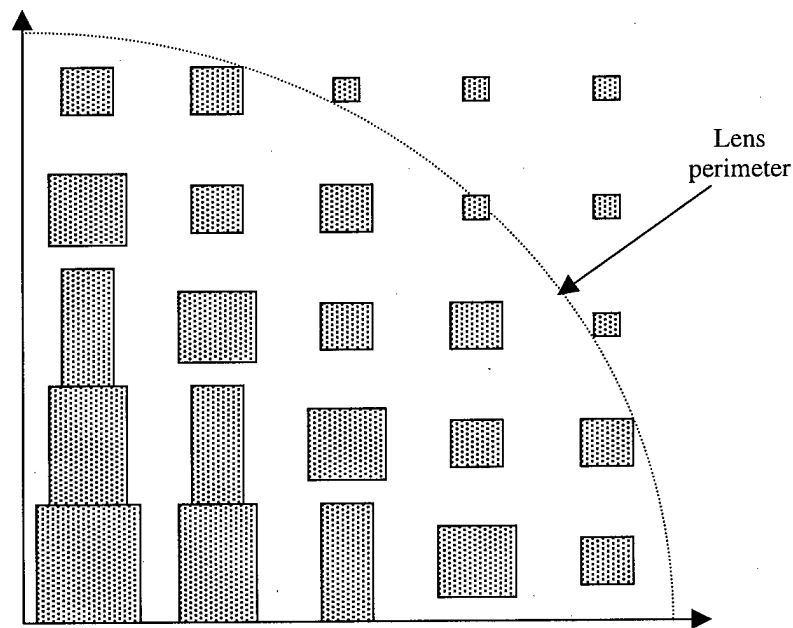


Figure 2.13. Hybrid 2-D/1-D fill-factor modulation method used to design a convex lens (top view of one quadrant)

modulation is used to provide maximum space between adjacent mesas. A minimum trench width (determined by the sophistication of the fabrication process) is used to calculate the transition point between the two methods. Two-dimensional fill-factor modulation is used once the space between mesas is sufficiently large. Such a hybrid approach may provide an optimum approach by making all horizontal features (mesas and trenches) at least  $3\ \mu\text{m}$ , which in turn significantly eases fabrication. Further improvement through reduction of diffraction effects may be possible by using trapezoids to define the one-dimensional fill-factor modulation section and circular pillars in the two-dimensional portion.

### 2.2.3 Other Etching Methods

While the above sections have presented several types of mass-transport pre-forms, they do not provide a comprehensive listing. As discussed at the beginning of Section 2.2, the mass in the pre-form can be arranged in any configuration provided that the horizontal sizes of pre-form features are small enough that they will be smoothed out during mass-transport. Other possibilities for pre-form types include a radially-symmetric one-dimensional fill-factor modulation approach, as shown in Figure 2.14. This closely resembles a Fresnel zone plate

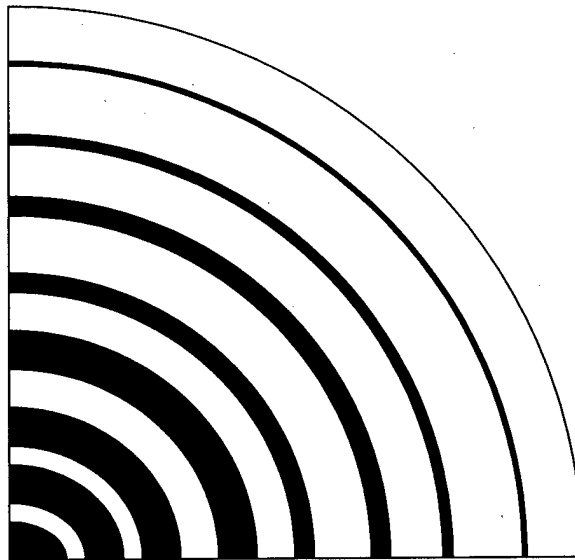


Figure 2.14. Radially-symmetric one-dimensional fill-factor modulation for convex lens; shaded region is unetched mesa (top view of one quadrant).

[Hecht & Zajac, 1987], which is composed of concentric rings that become thinner as their mean radius increases. This technique suffers from similar fabrication difficulties as the rectilinear one-dimensional modulation method due to the small width of mesas near the lens perimeter. This method also generates a circularly-symmetric lens, although removing the requirement of constant ring-width allows angular variation in the final surface.

The minimum width of the ring mesas can be increased by dividing the ring into segments, as shown in Figure 2.15. Similar to previous discussions, the arc length  $dS$  of each segment must be small enough that it will smooth out completely during transport. This method allows complete pixelization control of the final surface, though in this case the pixelization is in  $(r,\theta)$  rather than in  $(x,y)$ .

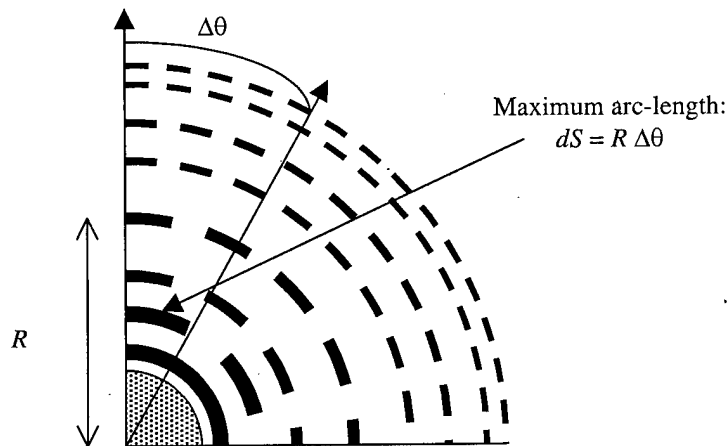


Figure 2.15. Segmented concentric ring pre-form to allow angular variation and larger ring width (top view of one quadrant).

Another possible variation of the pre-form pattern is to combine the multi-level and single-etch approaches, as shown in Figure 2.16. This allows the fabrication of elements with large sag without requiring a single etch that is larger than the sag. The small horizontal features and the large step are separate parts of the fabrication process. This introduces additional complexity to the fabrication, because either the small features must be patterned on a highly non-planar surface, or a large step must be added to the high-aspect-ratio pattern. Some of the techniques used to planarize large-aspect-ratio structures for further processing may prove beneficial for the realization of such structures [Stern & Medeiros, 1992; Horn, *et al.*, 1993].

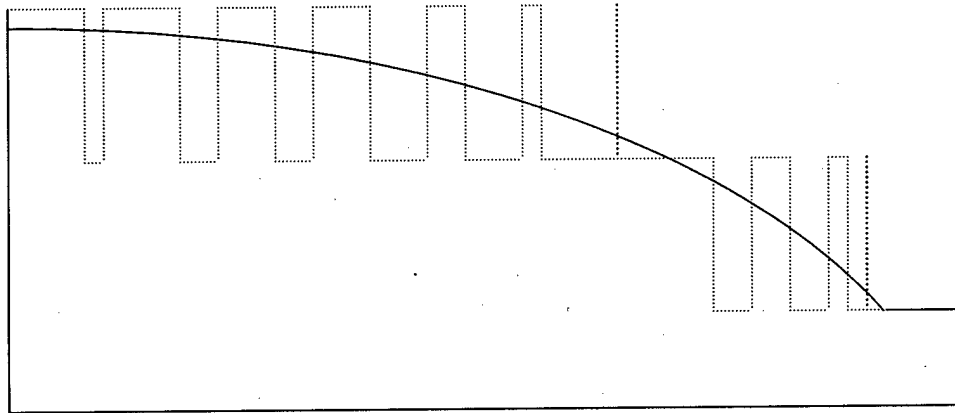


Figure 2.16. Combination multi-level and single-etch pre-form (side view);  
Before transport (dotted line) and after transport (solid line)

Throughout the above discussion of various pre-form design methods the effect of fabrication limitations upon each method has been apparent. It is clear that the minimum feature size or maximum aspect-ratio resolution of the fabrication technique used for the production of the etched pre-form impacts the size and/or  $f/\#$  of the optical element that can be made by mass-transport smoothing. Therefore, it can be expected that further improvements in fabrication techniques will allow the generation of more exotic optical surfaces of higher quality with less complex methods.

### 3. Experimental Methods

#### 3.1 Introduction

The mass-transport process begins with the construction of the GaP pre-form (as discussed in Chapter 2) which, following the mass-transport smoothing process, is transformed into the desired shape. This pre-form can be made by the process used to fabricate microelectronic integrated-circuits (ICs). The advanced technology used in IC fabrication allows the simultaneous production of many devices, each at relatively low cost [Campbell, 1996]. The microelectronic fabrication techniques most useful for the generation of mass-transport micro-optics are photolithography (which forms a masking pattern on the surface of the substrate) and

etching (which transfers the pattern into the substrate). The desired pattern in the chromium layer on a glass plate (the photomask) is reproduced in a thin layer of light-sensitive polymer (photoresist) applied to the top of the GaP substrate. This pattern is then transferred into the GaP substrate by an etching process. These two steps can be repeated as necessary to generate multiple levels with the requirement that each new layer be carefully aligned to the ones underneath. In the following sections each of the steps used to fabricate the GaP pre-form are discussed in general.

### 3.2 Mask Generation

After the desired optical surface has been designed and the particular pre-form type chosen it is necessary to make a photomask to act as a template for the reproduction of the pattern in the GaP substrate. The mask pattern is designed using a computer-aided drawing (CAD) package to generate a data file that is used by the mask fabrication service.

Masks fabricated by use of both scanning-electron-beam and optical-pattern-generation systems have been used in this research. The small diameter of the  $e$ -beam (typically  $<1 \mu\text{m}$ ) allows precise control of the feature size. The disadvantage of the  $e$ -beam technique is that the pattern is exposed in a raster-scan configuration; a mask area of several  $\text{cm}^2$  requires a long exposure time, thus increasing the mask cost. Masks made using an optical pattern generator, on the other hand, have reduced feature accuracy, but are less expensive as a result of the ability to form large rectangular features in a single exposure. With proper design compensation, masks made by use of optical-pattern-generation systems have been found to be of sufficient quality for the generation of mass-transport pre-forms.

### 3.3 Photolithography

The mask is then used as a template for the reproduction of the desired pre-form pattern in the GaP substrate. In the intermediate step of photolithography the mask pattern is reproduced on the surface of the GaP to form a protective layer used during the etching step.

Photolithography begins with a thorough cleaning of the GaP substrate. While surface contaminants may have a detrimental effect during the etching, the primary concern is the resolution of features in the lithography step. The GaP wafer (2-inch diameter) is cleaved into small pieces ( $\sim 1.5 \text{ cm} \times 1.5 \text{ cm}$ ) in this study; the cleaving process generates chips which often

adhere to the GaP surface. These chips create a non-planar surface that can introduce significant errors into the photolithography process through non-uniformity of the photoresist layer thickness. In addition, these chips move the mask out of contact with the substrate; this causes diffraction effects (which degrade the photoresist pattern) that are most severe for small mask features. Therefore, it is necessary to remove these chips by extended soaking of the GaP piece in solvents while subject to ultrasonic agitation.

After the substrate has been cleaned, positive photoresist is spin-coated at high rotational speed, resulting in a uniform, thin ( $\sim 1 \mu\text{m}$ ) layer. Following soft-baking to evaporate the residual photoresist solvent, the substrate is placed against the mask in a contact aligner. Good registration of each layer to those previously patterned is achieved by a set of chrome alignment marks deposited on the GaP surface during the initial fabrication step. A shutter controls the UV light exposure time for optimum resolution of features in the photoresist. Bonds are broken in the photoresist polymer by the UV radiation during exposure. The photoresist is then developed in a basic solution that dissolves the exposed photoresist without attacking the unexposed polymer. The exposure and development times have been optimized (generally at a minimum value) in this research for the best resolution of small features.

Further treatment of the photoresist prior to etching includes hard-baking (to evaporate the remaining solvent in the photoresist to make it more durable during etching) and  $\text{O}_2$ -plasma ashing (to remove thin photoresist scum layers from the substrate prior to etching).

### 3.4 Etching Methods

The photoresist pattern is then transferred into the GaP surface by an etching process that removes GaP from the exposed areas. A variety of different techniques for etching GaP exist, each having advantages and disadvantages depending upon the required etching speed, directionality, selectivity to masking material, *etc.* These techniques include isotropic processes such as wet-chemical etching and anisotropic processes, including reactive-ion-etching (RIE), ion-milling, and chemically-assisted ion-beam etching (CAIBE)

Chemically-assisted ion-beam etching (CAIBE) is similar to ion milling, *i.e.* a plasma ion source (either a Kaufmann or electron-cyclotron resonance source) is used to form a beam of accelerated Ar atoms. The CAIBE process, however, has an added chemical component that greatly increases its usefulness for the fabrication of microstructures. A reactive gas ( $\text{Cl}_2$  for the

etching of III-V materials) is sprayed over the sample surface and reacts spontaneously with the GaP [Hagberg, *et al.*, 1994]. At room temperature the  $\text{PCl}_3$  byproduct is volatile and rapidly desorbs from the surface; the  $\text{GaCl}_3$  byproduct is less mobile, however, and remains on the surface. The physical sputtering of the Ar beam removes the  $\text{GaCl}_3$ , exposing a fresh GaP surface for continued reaction. As a result, this technique gives independent control over the chemical and physical components of the etching process. Most importantly, the highly directional nature of the collimated argon beam results in anisotropic etching that yields vertical, smooth sidewalls. The CAIBE technique has been used in recent years to fabricate optical devices in the GaAs/AlGaAs system, including the gratings for grating-coupled surface-emitting lasers [Tiberio, *et al.*, 1990], the facets for in-plane lasers [Hagberg, *et al.*, 1992; Liang & Ballantyne, 1994], and numerous other optical structures. Reactive-ion-beam etching (RIBE) is a variation of the CAIBE technique; here a reactive species is substituted for the noble gas in the ion beam.

The CAIBE technique has been chosen to fabricate all pre-form structures in this research. This etching method provides a smooth surface with vertical sidewalls that most closely match the ideal pre-form designs described in Chapter 2. In addition, the CAIBE method has a large differential etch rate (GaP etch rate/photoresist etch rate). This permits the use of thin layers of photoresist for deep etching, which in turn improves the resolution of small horizontal features.

After etching, the remaining photoresist is removed with acetone and an  $\text{O}_2$ -plasma etch. If a multi-level pre-form is used, the photolithography and etching processes are repeated to define additional levels of the profile. A final etch step in the multi-level process creates a raised border around the pre-form structure that provides the proper spacing between the sapphire cover wafer and the GaP sample. The presence of the sapphire cover wafer minimizes surface porosity while the GaP-to-sapphire distance determines whether surface or vapor diffusion is the dominant transport mechanism. Removal of any chrome alignment marks complete the fabrication process.

### **3.5 Ampoule Cleaning and Sealing**

In this study mass-transport smoothing has been implemented using a sealed ampoule for greater safety and improved performance; the ampoule design is illustrated in Figure 3.1. The

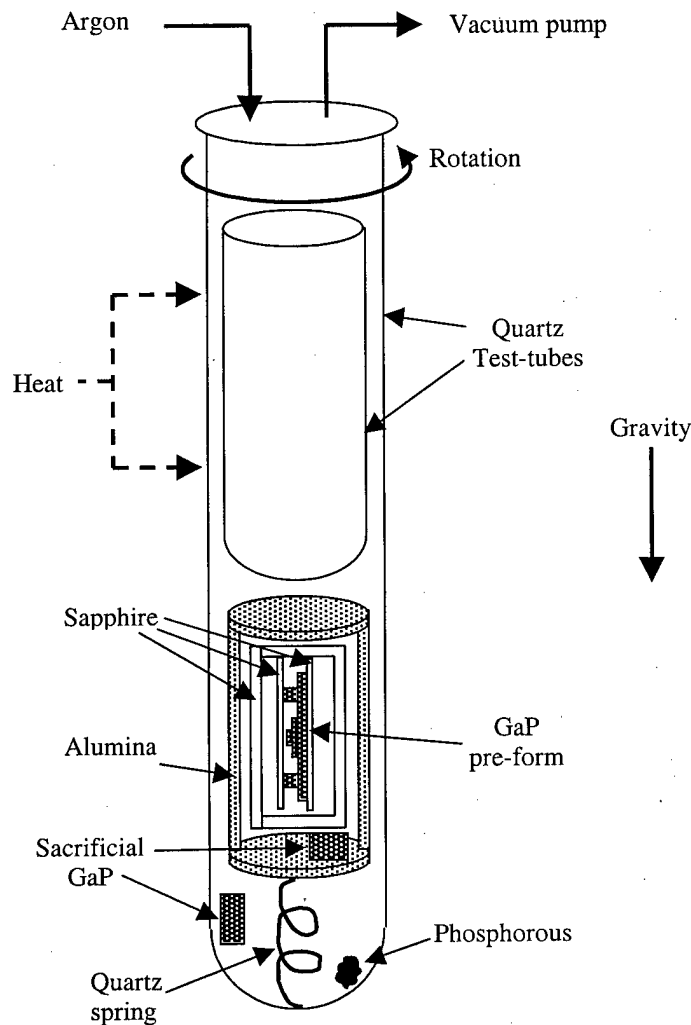


Figure 3.1. Diagram of mass-transport ampoule.

ampoule is a quartz test tube with a diameter of 28 mm and a length of 200 mm. The GaP wafer, sandwiched between polished sapphire plates, is placed into a sapphire box with lid. This box helps maintain contact between the sapphire cover plates and the GaP wafer during transport. This sapphire box is then placed into a cylindrical high-purity alumina (99.8%  $\text{Al}_2\text{O}_3$ ) crucible along with a small sacrificial piece of GaP. The sacrificial GaP acts as a supplemental source of phosphorous during mass-transport and attracts contaminants that might otherwise migrate toward the GaP pre-form and disrupt the transport process. A quartz spring, along with another sacrificial piece of GaP and a small piece of red phosphorus ( $\sim 0.5 \text{ mg/cm}^3$  of ampoule volume),

are placed into the bottom of the quartz test tube followed by the alumina crucible containing the GaP pre-form sample. The quartz spring compensates for the larger coefficient of thermal expansion of alumina relative to quartz and prevents ampoule rupture at high temperatures. A smaller quartz test tube (approximately 23 mm in diameter and 100 mm in length) placed inside the larger test tube provides a sealing point for the ampoule.

The mass-transport smoothing process is susceptible to degradation resulting from contamination; therefore it is necessary to thoroughly clean all ampoule parts before assembly and sealing. Each component of the ampoule is cleaned in an aggressive manner, though this cleaning is limited by the durability of each material. Following cleaning the ampoule is assembled in the order listed above and placed vertically into the sealing fixture.

The ampoule sealing fixture has two ports: one connected to a vacuum pump and the other to a cylinder of high-purity argon. These ports are in a stationary central shaft around which a cylinder rotates. This rotating cylinder is attached via an o-ring seal to the ampoule test tube. Before sealing the ampoule the test tube is heated (while rotating under vacuum) with a low-temperature  $H_2$  flame to bake off the water that adsorbed onto the surface of the ampoule parts during exposure to the atmosphere. Repeated evacuation and Ar purging between baking cycles flushes the water vapor out of the ampoule. The presence of water vapor in the ampoule is monitored with a pressure gauge; rising pressure during baking indicates continued water desorption, while a stable evacuated pressure of 30 - 50 mTorr during heating signals the complete removal of the water vapor. The ampoule is then filled with Ar to a pressure of 500 mTorr. The ampoule is sealed by heating the outer test tube with a high-temperature flame ( $H_2 + O_2$ ) as the ampoule rotates until the outer test tube collapses against the inner tube. Two identical seals (spaced by  $\sim 1$  cm) are made to guarantee the integrity of the ampoule.

### **3.6 Mass-Transport**

The sealed ampoule is placed inside of two larger cylindrical alumina crucibles and loaded horizontally into a three-zone tube furnace. The outer alumina crucibles provide a thermal baffle to minimize temperature non-uniformity in the furnace which leads to anisotropic diffusion. Level positioning of the GaP sample inside the ampoule helps to guarantee a good seal between the sapphire cover and the GaP sample surface. The furnace is equipped with a  $N_2$

flow as a safety precaution in case the ampoule breaks during transport and phosphorous is released.

The furnace temperature is increased at a rate of 2 - 3 °C/min up to 1100 °C. This slow ramp rate is necessary so that mass-transport smoothing does not proceed too quickly on the etched pre-form while it still has sharp edges. By the time the maximum temperature is reached and mass-transport is occurring at the fastest rate, some initial transport will have smoothed the highest spatial frequency components. A slow temperature ramp-rate also minimizes temperature gradients across the sample surface which reduces the possibility of non-uniform smoothing. The furnace temperature remains at 1100 °C for 20 - 50 hours depending upon the desired amount of diffusion. The temperature is then decreased at a rate of 2 - 3 °C/min to 800 °C to gradually halt the diffusion process. At this point the furnace is turned off and rapidly cooled (~5 °C/min) to 300 °C.

The ampoule is removed from the furnace and one end placed into acetone. This rapid quenching causes condensation of the phosphorous (now converted into pyrophoric white phosphorous) at the coolest end of the ampoule. When the ampoule is broken open the phosphorous hazard is confined to a small region of the ampoule and is easy to handle. The GaP pieces are detoxified in n-methyl-2-pyrrolidone; all other parts are cleaned in heated dilute Aqua Regia.

## **4. Experiments**

### **4.1 Overview**

The experimental work of this project is described in this chapter. Section 4.2 describes the fabrication and testing of a Fresnel biprism using a multi-level pre-form, while Section 4.3 discusses the fabrication and testing of an off-axis lens using a binary pre-form. The results from the experiments in Sections 4.2 and 4.3 have been published previously [Ballen & Leger, 1999]. Section 4.4 describes the use of a concave mirror (fabricated by mass-transport) to control the spatial-mode performance of a VCSEL and the replication of that mirror (as well as the biprism discussed in Section 4.2) in GaAs [Nikolajeff, *et al.*, 1999]. Section 4.5 discusses an experiment used to test the surface and vapor diffusion processes. Section 4.6 describes an experiment in which the surface roughness of a replicated GaP microlens was reduced by mass-transport.

Section 4.7 describes the effects of etching errors in the pre-form fabrication process upon the final surface; an example of an experiment to calibrate the undercutting is included. Finally, Section 4.8 demonstrates a distortion-free optical interconnection system using an array of off-axis GaP microlenses.

## 4.2 Fresnel Biprism

Prismatic optical surfaces have applications in beam-steering and interferometry. Unlike simple convex microlenses (that can be made by use of virtually all of the available micro-optical fabrication techniques), prisms can be fabricated using only a few of these techniques (including mass-transport). Therefore, the mass-transport fabrication of a prism is used to demonstrate the ability of the smoothing process to make high-efficiency optical elements with nontraditional surfaces.

Using the "equal mass" method described in Section 2.2.1 it is apparent that a pre-form containing steps of equal height and width generates the desired flat prismatic surface following mass-transport. The back side of a regular prism, however, does not remain vertical during mass-transport due to step broadening. While this broadening might be thought to severely degrade the optical performance of the surface only in the case of a blazed grating structure (where 100% of the area is used and there are no "dead" regions), the regular prism suffers as well. During mass-transport a large vertical discontinuity gradually broadens, or bends over, as the parts of the surface profile decay. The decay of the small spatial-period components also creates ripples in the surface above and below the discontinuity, as shown in Figure 2.1a. In the case of a prism these ripples are present on the useful portion of the prism and cause significant aberration. Therefore, a Fresnel biprism was chosen as a demonstration structure because its inherent symmetry reduces the effects caused by large vertical discontinuities.

A Fresnel biprism was designed using a multi-step mass-transport pre-form with five steps, each with a width of 20  $\mu\text{m}$  and a height of 1.57  $\mu\text{m}$ . As a result of the high index of GaP ( $\sim 3.17$ ), this method results in a transmission deflection angle (for a beam that is incident normal to the prism base) of  $10.2^\circ$ . The GaP pre-form was fabricated using the methods described in Chapter 3. A reproducible etch rate in the CAIBE system allowed each level to be etched with an rms etch-depth error of 3.5%. Increased accuracy could be obtained by a partial etch (*e.g.*, 90% of the depth), followed by a measurement and a corrected final etch. A raised border of a

height of  $3.5\ \mu\text{m}$  was added to each sample for proper cover-wafer spacing. Adequate mass-transport of one sample occurred with the technique described above after 34 hours. The mass-transport process resulted in nearly complete smoothing of the  $20\text{-}\mu\text{m}$  steps; a second sample, transported for 59 hours, showed a similar degree of smoothing. It is thought that the transport process is being inhibited by the presence of contamination from the quartz ampoule [Swenson *et al.*, 1995]. This contamination can most likely be reduced and the effective transport length

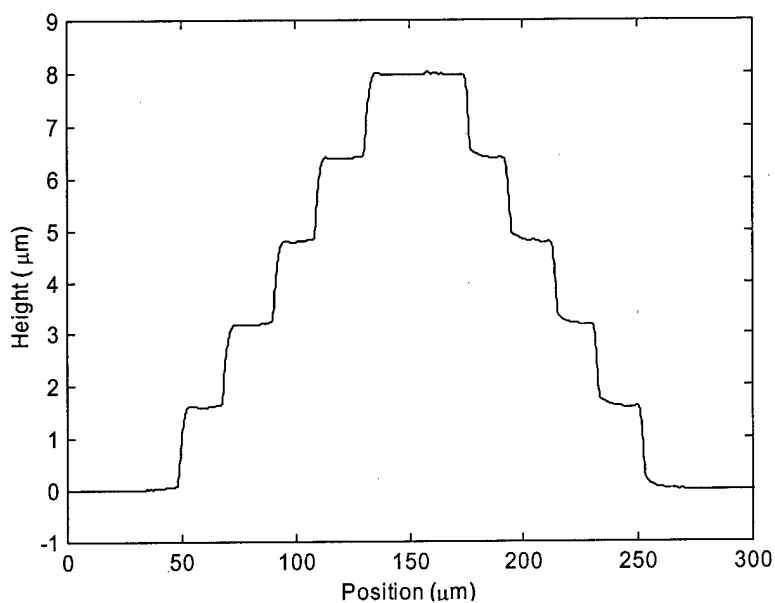


Figure 4.1. Surface profilometer data for GaP biprism pre-form before transport.

extended by improving the seal between the sapphire cover wafer and the GaP. In both cases, however, the GaP was smooth and optically transparent after mass-transport.

Plots from a stylus profilometer showing the mass-transport pre-form and the smoothed biprism are shown in Figures 4.1 and 4.2, respectively. Because the stylus tip has a radius of  $5.0\ \mu\text{m}$ , an abrupt step of  $\sim 1.6\ \mu\text{m}$  height is broadened by  $\sim 3.7\ \mu\text{m}$  by the profilometer. With the exception of a small amount of residual ripple, the steps are observed to have smoothed completely. The biprism was further characterized with a white-light scanning interferometric microscope to measure the surface figure. The surface profile data (shown in Figure 4.3) emphasizes the quality and uniformity along the length of the prism.

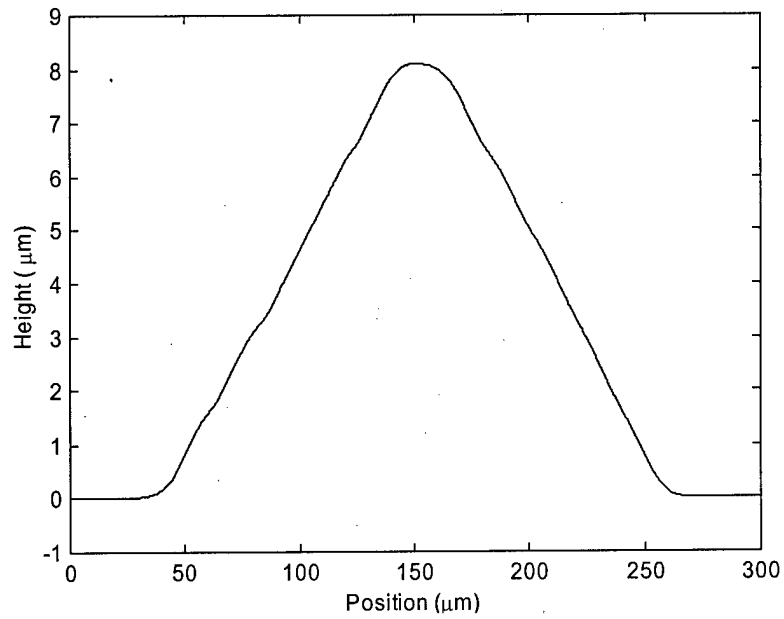


Figure 4.2. Surface profilometer data for GaP biprism after transport.

After completion of surface profile measurements, a multi-layer anti-reflection coating ( $R < 1\%$  at  $\lambda = 0.633 \mu\text{m}$ ) was applied to both sides of the GaP substrate prior to optical testing.

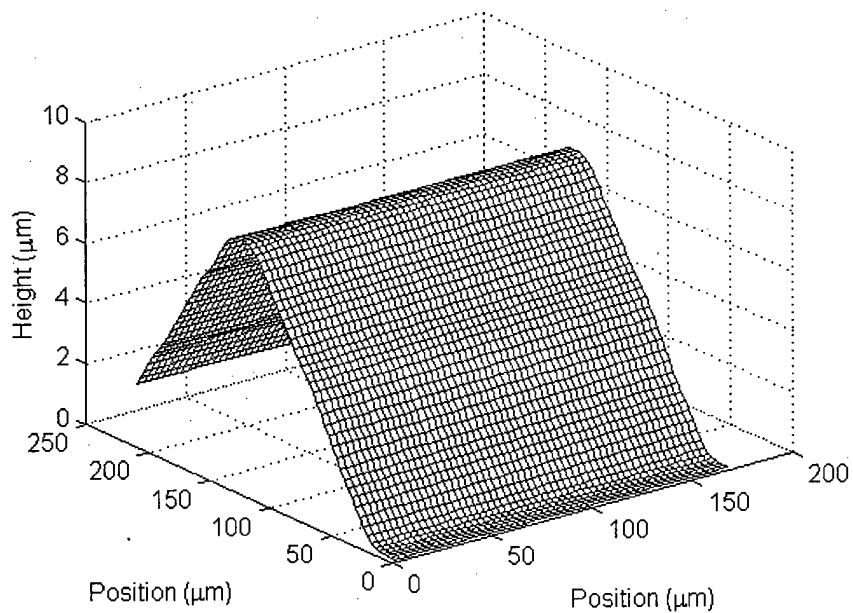


Figure 4.3. Scanning white-light interferometric microscope data for GaP biprism after transport.

The biprism was then placed into the optical system shown in Figure 4.4. Light from a He-Ne laser was spatially-filtered and collimated before being used to illuminate an aperture. An afocal imaging system was used to form a demagnified image of this aperture on the GaP biprism. The spot size of the beam at the GaP surface was measured to be  $\sim 35 \mu\text{m}$ . Accurate positioning of the afocal system along the optical axis was possible with the aid of a transparent resolution target and a microscope.

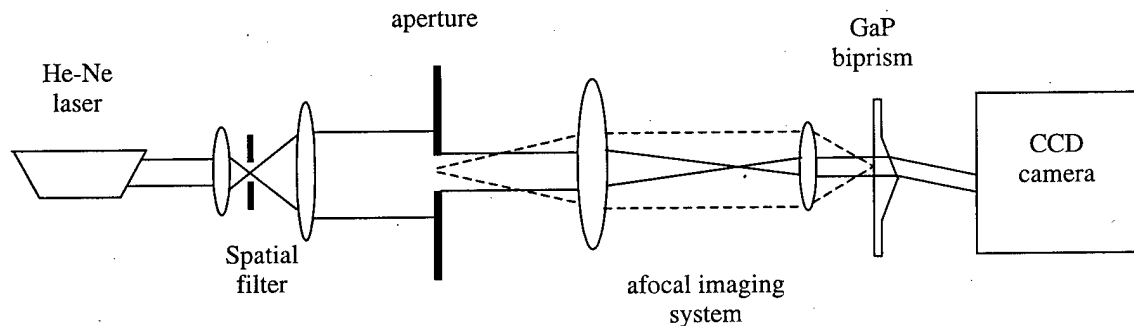


Figure 4.4. Experimental set-up for testing beam-steering of GaP biprism with normally-incident He-Ne beam.

Translation of the GaP substrate so the beam strikes either of the two biprism faces or a flat region of the substrate caused the beam to be steered in three distinct directions. The beam deflection angle (when striking either of the biprism faces) was measured to be  $\sim 11.5^\circ$ , which is larger than the expected value of  $10.2^\circ$ . The predicted value can be corrected by measurement of the actual base angle of the biprism. Measurements taken from the stylus data shown in Figure 4.2 yield a base angle of  $4.9^\circ$  (instead of the predicted  $4.6^\circ$ ) leading to a corrected beam-steering angle of  $10.9^\circ$ . This increase in base angle is the result of slight over-etching of several of the pre-form steps. This adjustment provides better agreement between the measured and expected values but also highlights the strict fabrication tolerances present with a material of such high refractive index.

Far-field images for the three beam positions were recorded at a distance of 5.0 cm after the GaP substrate by use of a CCD camera with a frame-grabber. In each case the far-field intensity of the beam had a clean, Airy-disk form. The combined data for the three beam

positions are displayed in Figure 4.5. Comparison of either deflected beam with the central undeflected beam indicates the negligible aberration introduced by the prism surface.

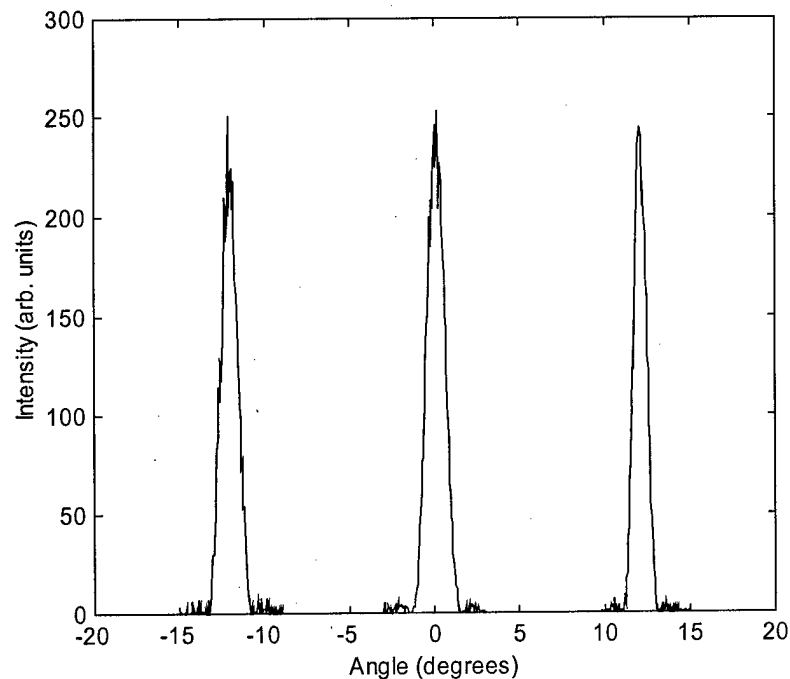


Figure 4.5. Far-field intensity data for He-Ne beam steered to three locations by GaP biprism.

A power meter was used to measure the overall power efficiency of the structure. Comparison of the beam power through a flat etched-and-transported section of the substrate with the incident power yielded a loss due to absorption, scattering, and reflection of  $\sim 2\%$ . The power at the two steered locations was measured for several propagation distances beyond the GaP substrate. This deflected power was then compared with the incident power to calculate an overall power efficiency that accounts for all losses. This efficiency was measured to be  $>94\%$  for several propagation distances and rose to  $\sim 96\%$  for propagation distances less than 5.0 cm. This small variation in efficiency is likely caused by small-angle scattering from large-period distortions in the prism surface. These ripples are caused by incomplete smoothing of the pre-form steps, or are the residual effect of slight layer misalignment during fabrication [Liau, *et al.*, 1994d].

### 4.3 Off-Axis Lens

Off-axis lenses are useful for a variety of applications requiring beam-steering, such as optical interconnection systems (which are described in detail in Section 4.8). Off-axis lenses can also be used to reconfigure light to more efficiently illuminate a desired region. The geometrical transformation of a linear diode-laser array using an array of off-axis lenses has been proposed using diffractive [Leger & Goltsos, 1992] and refractive microlenses [Ballen & Leger, 1998]. The aspheric profile of an off-axis lens provides another opportunity to emphasize the versatility of the mass-transport fabrication to make arbitrary optical surfaces.

The aspheric off-axis lens surface was modeled as a 10th-order polynomial in rectangular coordinates. A lens design code (Code V<sup>TM</sup>) was used to optimize the surface for the collimation and off-axis steering of light from a point source. A binary pre-form to produce this surface following mass-transport was then designed (as described in Section 2.2.2) and etched into a GaP substrate.

The FFT computational method described in Section 2.1 was used to simulate mass-transport smoothing of a binary pre-form to generate an off-axis lens. The simulation results are shown as a cross-section through the center of the lens in Figure 4.6. An  $f/1.5$ , 200- $\mu\text{m}$  diameter

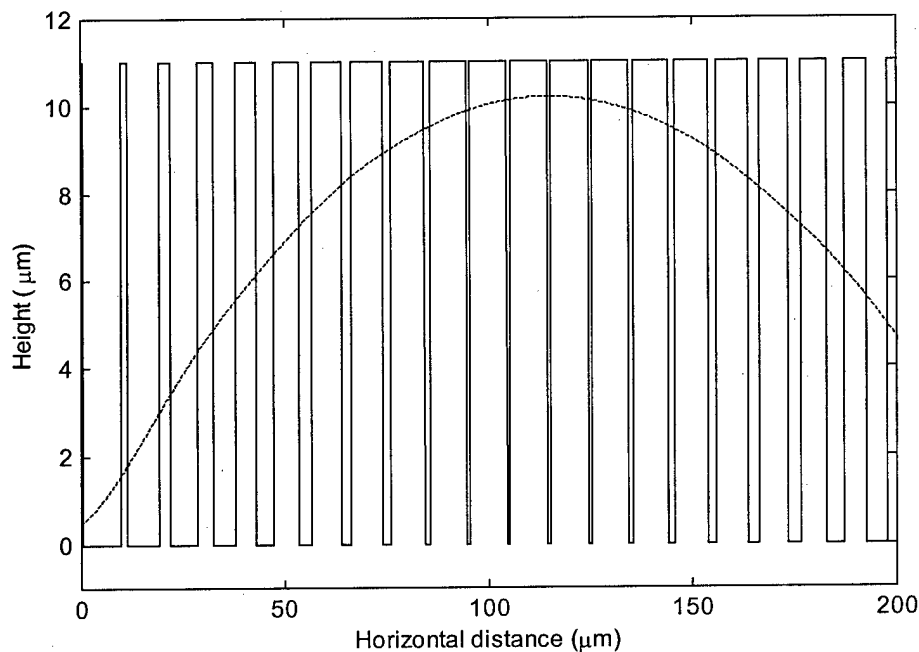


Figure 4.6. Simulated smoothing of a binary pre-form to generate an off-axis GaP lens ( $f/1.5$ , 200- $\mu\text{m}$  diameter,  $2.9^\circ$  steering angle) shown in cross-section. The solid line is the etched pre-form; the dashed line is the resulting surface after simulated mass-transport.

off-axis GaP lens was optimized as a 10th-order polynomial in rectangular coordinates to collimate a point source and deflect the collimated beam at an angle of  $2.9^\circ$ . The etched pre-form is shown as a solid curve, the smoothed profile as a dashed line. The optical path difference between the smoothed profile and the desired optical surface across the middle 80% of the lens is  $\sim\lambda/20$  (rms.), corresponding to a Strehl ratio of  $\sim 90\%$ .

A similar lens pre-form was designed ( $f/2.0$ ,  $150\ \mu\text{m}$ -diameter,  $2.9^\circ$  off-axis) and fabricated using a single step of photolithography and etched into a GaP substrate using the CAIBE system. The GaP pre-form was cleaned and sealed into an ampoule, which was placed into a furnace and transported at  $1100\ ^\circ\text{C}$  for 24 hours. The surface of the resulting lens is shown in cross-section in the stylus profilometer data displayed in Figure 4.7, where the dotted line is the theoretical etched pre-form, the solid line is the measured surface, and the dashed line is the theoretical surface computed by simulated smoothing of the pre-form using the FFT

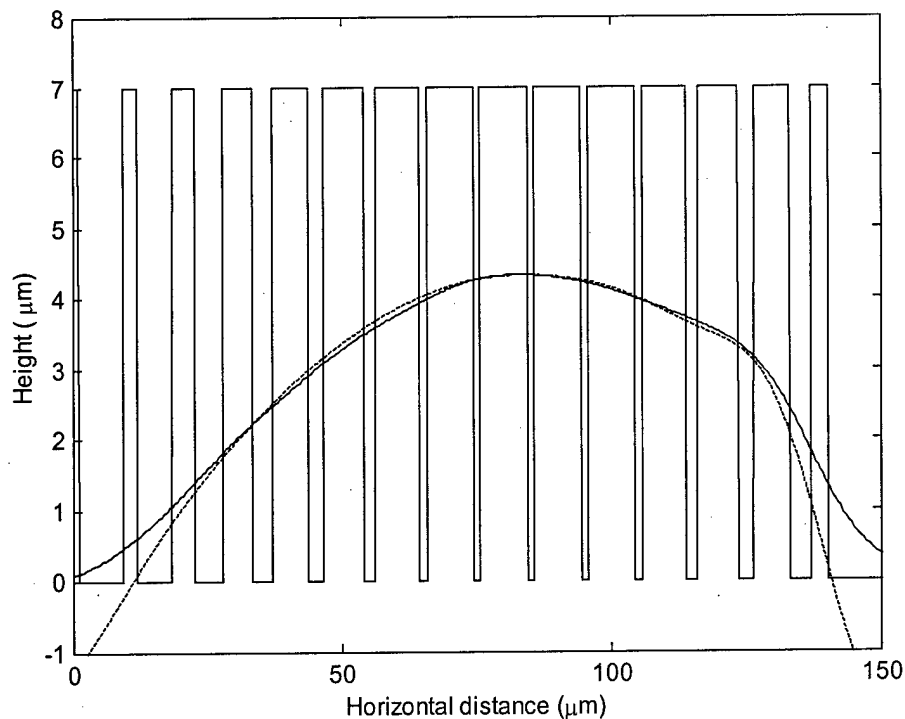


Figure 4.7. GaP off-axis lens ( $f/2.0$ ,  $150\ \mu\text{m}$ -diameter,  $2.9^\circ$  steering angle): square-edged solid line is theoretical etched pre-form, smooth solid line is measured surface profile, dashed line is theoretical prediction including approximate effects of uniform undercutting of pre-form.

computational technique described in Section 2.1. In this case, the theoretical surface has been shifted down to approximate the effects of a non-ideal etched pre-form caused by uniform undercutting. (The effects of etching errors in the binary pre-form on the final lens profile are discussed below in Section 4.7.) As can be seen in Figure 4.7, the measured profile closely matches the theoretical profile in the center of the lens. Also, the optical path difference between the measured profile and the desired optical surface across the middle 50% of the lens is  $\sim\lambda/12$  (rms.). Of particular interest is the presence of the bump on the right side of the lens in both curves. This distortion is the result of an error in the design of the pre-form. The off-axis lens in this study can be thought of as the sum of a standard convex lens and a prism. Such a surface has a large vertical discontinuity (equal to the height of the prism) at one edge of the lens. This discontinuity was included in the design of the lens pre-form. During mass-transport, however, all vertical steps "broaden" as the higher spatial frequency components decay. This broadening results in a convex bump at the top of the step and concave dip at the bottom; it is this bump which is present at the edge of the off-axis lens. This distortion can be avoided, however, by extending the optical surface (and thus the pre-form pattern) beyond the perimeter of the lens. While this added portion of the lens would not be used in the optical system, its presence removes the edge effects caused by a large vertical discontinuity.

The optical properties of this lens were measured by collimating a point source generated from a semiconductor laser ( $\lambda = 850$  nm). The measured deflection angle of the collimated beam matched the desired angle ( $\sim 2.9^\circ$ ). As a result of the distortion at the right side of the lens, full illumination of the lens would result in degradation of the far-field diffraction pattern. Therefore, an aperture was used to restrict the illumination to only the central half of the lens, effectively increasing the  $f/\#$  of the lens. A cross-section of the far-field intensity pattern for this partial illumination is shown in Figure 4.8. The angular width of this pattern ( $\sim 0.8^\circ$ ) corresponds to a diffraction-limited divergence for a  $75 \mu\text{m}$  aperture.

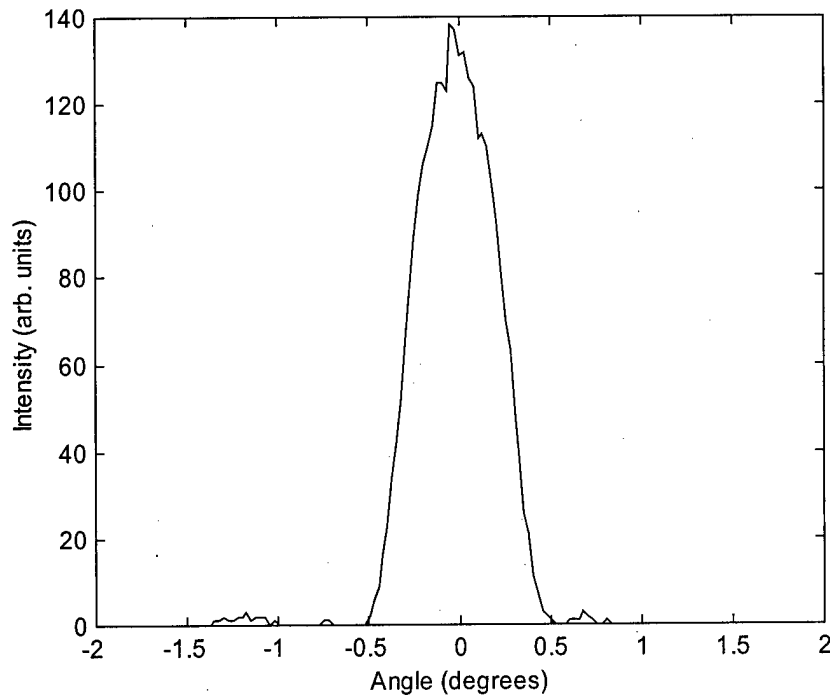


Figure 4.8. Far-field intensity data for GaP off-axis lens.

#### 4.4 VCSEL Spatial-Mode Control

Vertical-cavity surface-emitting lasers (VCSELs) are attractive as light sources due to their desirable properties, including circular mode profile, single longitudinal mode operation and output perpendicular to the wafer surface. In addition, large two-dimensional arrays can be fabricated with relative ease, and on-wafer testing can be performed to measure device quality before packaging. A VCSEL consists of an epitaxially-grown bottom mirror formed by alternating layers of GaAs and AlGaAs, one or more quantum wells of  $\text{Ga}_x\text{In}_{1-x}\text{As}_y\text{P}_{1-y}$  (with  $0 \leq x, y \leq 1$  chosen to emit the desired wavelength), and an epitaxially-grown top mirror. Because the length of the active region of a VCSEL is typically only  $\sim 10$  nm, the round trip gain is small and high-reflectivity mirrors are required to achieve continuous-wave (cw) lasing at room temperature. The spatial modes supported by the VCSEL cavity are determined by the interaction between the effects of current flow, thermal lensing, and spatial hole burning. The size of the VCSEL aperture greatly influences these effects, with aperture diameters ( $1/e^2$ ) of less

than 5  $\mu\text{m}$  required for single-spatial-mode operation. Consequently, the small overall gain volume of a single-mode cw VCSEL generally restricts it to a maximum power of only a few milliwatts.

In many applications such as optical storage and high-speed optical communication high-power single-transverse-mode output is desirable. To increase the power from such devices research has been directed toward either reducing the operating voltage (thus reducing thermal effects) or providing modal discrimination inside or outside the laser cavity. With proper modal discrimination large-aperture VCSELs can be used, leading to an increase in single-spatial-mode power. There have been several attempts to increase modal discrimination by spatial filtering. Conventional macroscopic laser mirrors have been used to provide additional feedback in the far-field, providing modal discrimination by introducing larger losses to the higher-order modes [Hadley, *et al.*, 1993; Wilson, *et al.*, 1993]. A second approach uses a graded-index lens and performs the spatial filtering in the back focal plane of the lens [Koch, *et al.*, 1997]. Finally, an integrated spatial filter has been used to filter the modes in the near-field [Morgan, *et al.*, 1993]. In this experiment spatial mode control of a VCSEL has been accomplished with a concave GaP micromirror (fabricated using mass-transport). The mirrors are tested in an external cavity configuration and shown to induce single mode operation in large-aperture VCSELs over a wide range of currents.

#### 4.4.1 Spatial Filtering with Micromirrors

The approach for spatial mode control used in this demonstration relies on an integrated micromirror to spatially-filter the VCSEL output beam in the far-field. The diameter of the mirror is chosen to reflect most of the fundamental mode, while it simultaneously clips enough of the higher-order modes to prevent these from lasing. By using miniaturized optics the additional mirror can be integrated with the VCSEL structure. The micromirror can be placed either on the top or bottom surface of the VCSEL substrate, depending on the type of VCSEL. Figure 4.9 shows a configuration that is appropriate for an InGaAs VCSEL with a wavelength of 980 nm. Since GaAs is transparent at this wavelength, the micromirror can be integrated onto the back side of the substrate, and the useful output light can emit from the top. In this figure, the bottom distributed Bragg reflector (DBR) mirror of a conventional VCSEL is not present; the cavity is formed between the curved micromirror and the top DBR mirror. Of course, the

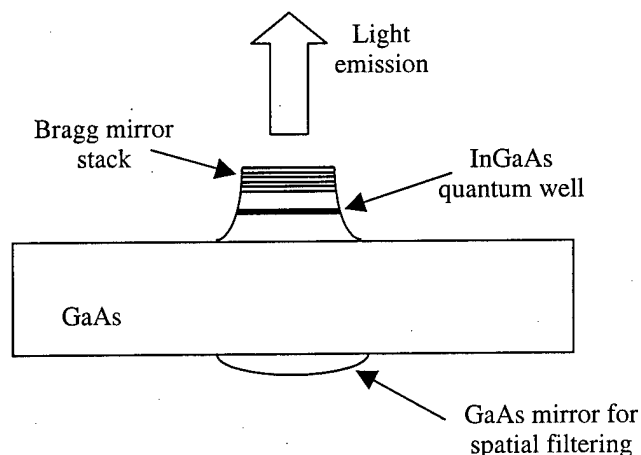


Figure 4.9. Micromirror integrated with an InGaAs VCSEL for spatial-mode discrimination through spatial filtering in the far-field.

reflectivity and optical performance of the curved mirror must be very high to allow efficient lasing. In addition, this configuration will have several longitudinal modes that fall within the gain curve of the cavity. An alternative design retains a partial-reflecting bottom DBR mirror stack to form a conventional VCSEL cavity. The reflectivity of the bottom stack is reduced, however, so that the VCSEL will not lase without additional feedback from the curved mirror.

The far-field condition together with the finite thickness of the substrate place a limit on the fundamental mode size. The micromirror is located in the far-field only when the propagation distance is much greater than the Rayleigh range. Thus, the mode half-diameter  $\omega_0$  is restricted by the requirement:

$$\omega_0 \ll \sqrt{(\lambda z_0 / \pi n)} \quad (4.1)$$

where  $z_0$  is the propagation distance from the VCSEL aperture to the micromirror,  $\lambda$  is the wavelength of light in free space, and  $n$  is the index of refraction of the propagation medium (GaAs). Evaluation of Equation 4.1 with representative numbers for  $z_0$  (1000  $\mu\text{m}$ ),  $\lambda$  (0.98  $\mu\text{m}$ ), and  $n$  (3.5) results in an upper limit on  $\omega_0$  of 9.4  $\mu\text{m}$ , or a mode diameter ( $1/e^2$ ) of approximately 19  $\mu\text{m}$ . For larger diameter VCSELs, one can either increase the propagation distance (making integration difficult with substrates of standard thickness), use a microlens to produce the far-field, or use special techniques for spatial-filtering in the near-field [Chen, *et al.*, 1999; Leger, *et al.*, 1994]

To test the GaP micromirrors a top-emitting VCSEL has been used in an external cavity configuration. An external cavity configuration was chosen instead of integrating the mirror with the VCSEL because the former technique allows us to test the performance of the micromirror for different laser beam magnifications using the same VCSEL. Furthermore, a moveable micromirror allows easier investigation of tolerance to misalignment.

The VCSEL is a conventional AlGaAs structure (emission wavelength = 850 nm) which has a reduced top DBR mirror stack of six periods with a calculated reflectivity of 95%. The micromirror was designed to provide the additional external feedback necessary for lasing to occur. The mirror should be placed in the far-field and its aperture made small enough that sufficient feedback for lasing is provided only to the fundamental mode. For efficient feedback the surface profile of the mirror must match the wavefront of the laser beam and reflect the beam back to the VCSEL. The fundamental mode of the VCSEL is assumed to have Gaussian profile with its waist formed at the top DBR mirror stack. A Gaussian beam propagating in the far-field has a spherical wavefront; the radius of curvature of the GaP mirror is thus set equal to the radius of curvature of the wavefront at the mirror plane. A distance  $z_0 = 2$  mm was chosen for the spacing between the VCSEL aperture and the micromirror. Since the propagation medium in this configuration is air, Equation 4.1 requires that the VCSEL mode waist  $\omega_0 \ll 23$   $\mu\text{m}$ . This condition was met for all VCSELs used in this experiment.

The micromirror was designed for a VCSEL with a 15- $\mu\text{m}$  diameter aperture. This aperture size is large enough that the VCSEL (without spatial filtering) should begin to lase in multiple modes almost immediately as the drive current is increased above threshold. In order to determine the mode size at the micromirror it is necessary to know how large the mode is at the VCSEL. As was mentioned above, the actual mode size is determined by a number of factors. By using the VCSEL aperture size as an upper limit on how large the mode size can be, the mode size at the mirror plane can be calculated. If the actual mode size at the VCSEL is smaller than the aperture size then the mode at the mirror will be larger than expected and the micromirror will filter even more of the beam. With a beam half-diameter of 7.5  $\mu\text{m}$  at the waist the beam diameter is calculated to be 145  $\mu\text{m}$  at a distance of 2 mm from the VCSEL (10 times the Rayleigh range). It is not directly obvious how large the aperture of the mirror should be relative to the beam size for the most efficient filtering to occur without introducing excess loss to the fundamental mode. The maximum intensity value of the second-order mode is located at the

radial distance where the intensity of the fundamental mode has dropped to  $1/e^2$  of its maximum value. It is therefore reasonable to make the mirror diameter equal to the beam width of the fundamental mode (145  $\mu\text{m}$ ). In the far-field region the radius of curvature of a Gaussian beam is approximately given by its propagation distance; thus the radius of curvature of the mirror was chosen to be 2 mm. This results in a mirror with an  $f/\#$  of 6.9 and a Fresnel number  $N = 3.1$ , where the Fresnel number has been defined as

$$N = a^2 / \lambda z_0 \quad (4.2)$$

with the mirror radius given by  $a$ . Note finally that it is necessary to make the micromirror concave because it is used in a coupled-cavity configuration with a top-emitting VCSEL. If the mirror were integrated with the VCSEL it would be concave from the inside and thus a convex mirror would be required on the bottom surface of the substrate (as shown in Figure 4.9).

The micromirror was fabricated in GaP using mass-transport smoothing. A single-etch pre-form with one-dimensional mesa-width modulation (described in Section 2.2.2) was fabricated using the techniques discussed in Chapter 3. Unlike the typical case of a convex lens described in Section 2.2.2, the pre-form for the concave mirror consists of a series of parallel trenches that are widest in the center (near the deepest part of the mirror) and become narrow at the mirror edge. This structure is therefore the complement of the pre-form used to generate a convex lens. The GaP pre-form was cleaned, placed into a sealed ampoule, and heated at 1100

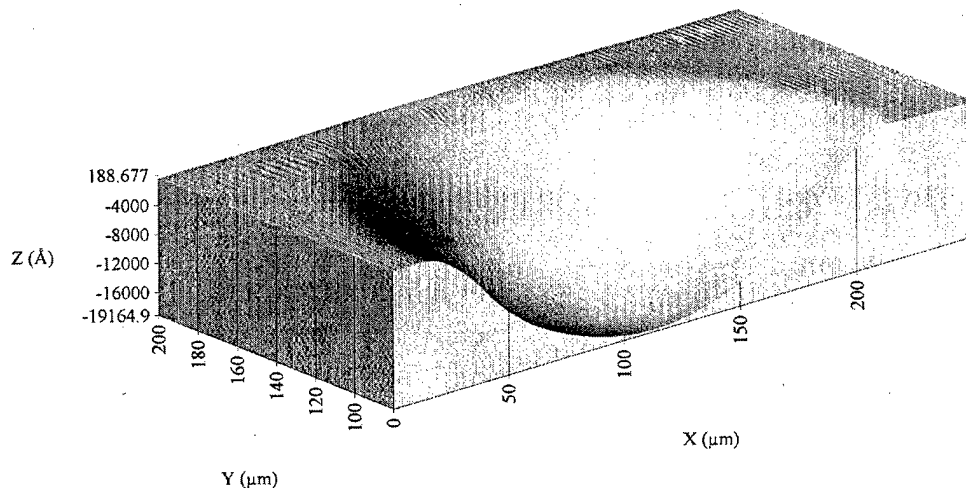


Figure 4.10. Profilometer measurement of a portion of the fabricated GaP concave micromirror.

°C for 24 hours to generate the smoothed mirror. Following characterization of the mirror figure it was coated with a reflective gold layer of 120 nm thickness.

Figure 4.10 shows a profilometer measurement of a portion of the fabricated GaP mirror. As can be seen, the desired concave shape has been achieved and the finished surface is smooth with no trace of the pre-form pattern. The sag of the mirror is  $\sim 1.9 \mu\text{m}$ . Figure 4.11 shows a trace through the center of the mirror. The measured profile closely matches a sphere with a radius of curvature of 2.25 mm. The discrepancy between the experimental and the design radius of curvature (2 mm) can be attributed to incomplete etching of the GaP pre-form, which was caused by a lower GaP etch rate than expected. The optical path difference between the measured profile and the sphere is  $\sim \lambda/30$  (rms).

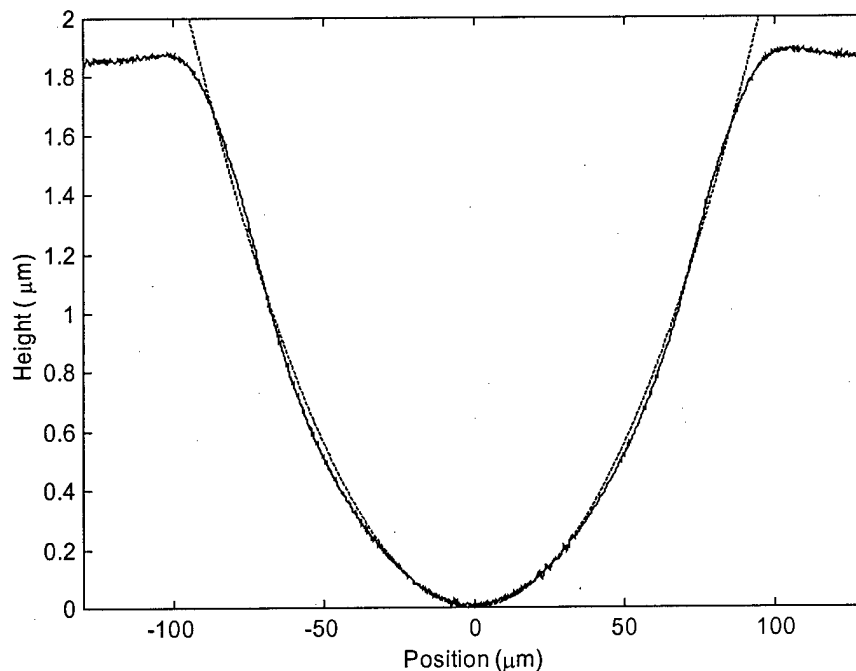


Figure 4.11. Profilometer trace through the center of the GaP micromirror (solid line); spherical fit (with radius of curvature = 2.25 mm) to data (dotted line).

To test the optical performance of the GaP micromirror, an afocal system composed of two antireflection-coated lenses was used to image out the VCSEL plane (see Figure 4.12). One advantage of using an afocal optical system in this test is that the magnification can be easily changed to simulate the effect of micromirrors with varying Fresnel numbers. The micromirror

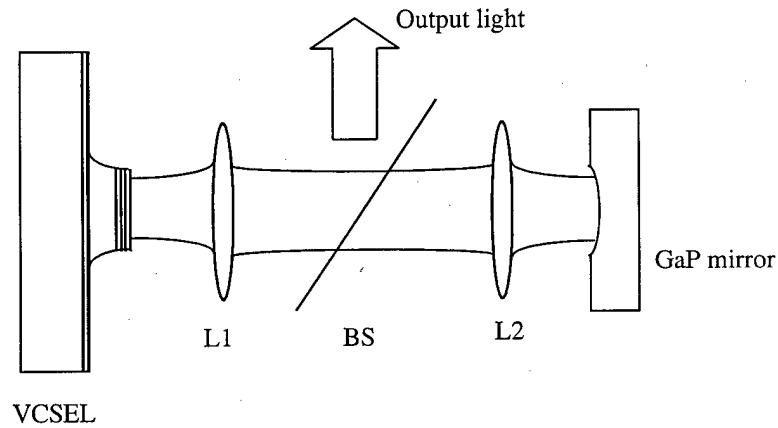


Figure 4.12. Experimental arrangement used to test the micromirror. The afocal system (L1 and L2) images the VCSEL onto the micromirror. Varying the focal lengths of the two lenses allows different beam magnifications to be obtained. A beam splitter (BS) couples light out of the cavity.

is placed in the focal plane of the second lens. The afocal system also forms an image of the micromirror plane at the VCSEL. A beamsplitter is placed between the two lenses to couple light out of the cavity. The VCSEL plane can thus be imaged out of the cavity and monitored. This configuration facilitates alignment of the micromirror by allowing simultaneous viewing of the micromirror and VCSEL planes. When the surface of the mirror is placed exactly in the image plane of the afocal system, the center of the concave micromirror reflects an image of the VCSEL and no spatial filtering is achieved. This configuration produces a low current threshold and allows a misalignment tolerance of  $\sim 50 \mu\text{m}$  in the transverse direction. However, as the driving current of the VCSEL is increased, the VCSEL almost immediately begins to lase in multiple spatial modes. When the mirror is moved along the optical axis away from the focal plane the lasing ceases until the mirror reaches a location of  $\sim 2.2 \text{ mm}$  behind the focal plane, at which point the VCSEL starts to lase again. This is in good agreement with what is expected from the estimated radius of curvature of the fabricated GaP mirror. The tolerance to misalignment in this plane is approximately  $120 \mu\text{m}$  in the longitudinal direction but only a few micrometers in the transverse directions.

The out-coupled light was measured with a spectrometer. Figures 4.13 and 4.14 show the spectra for various drive currents both when the mirror is placed in the image plane of the afocal system and when the mirror is placed 2.2 mm behind the image plane. Because each spatial mode has a different characteristic wavelength, multiple modes will be evident by separate lines in the spectrometer. The threshold current for the configuration with the mirror in the afocal image plane is 5.9 mA. In this case the VCSEL breaks into multimode operation at a drive current of  $1.6 I_{th}$  (see Figure 4.13). When the mirror is moved to the far-field of this image (2.2 mm away), the finite size of the mirror acts as a spatial filter and the threshold current increases to 7.0 mA. An increase in threshold current is expected since part of the reflected beam is

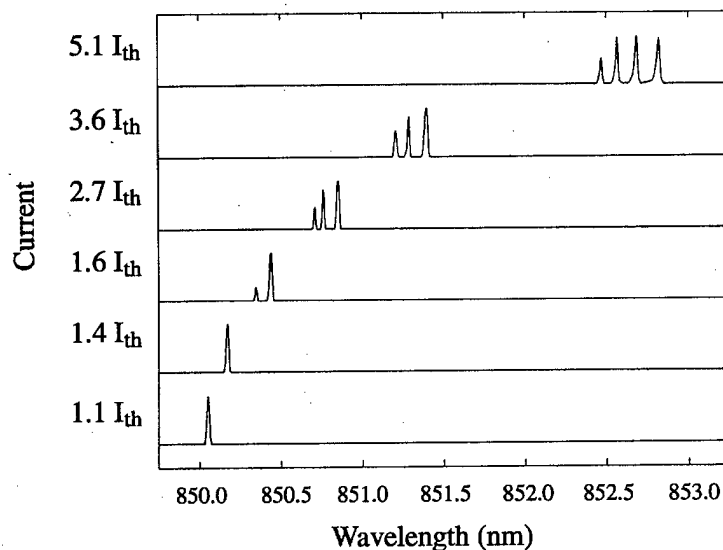


Figure 4.13. Spectral data for a 15- $\mu\text{m}$  VCSEL without spatial filtering; the VCSEL becomes multimode at a drive current of  $1.6I_{th}$ .

blocked. However, the VCSEL now operates in a single spatial mode for currents up to more than  $6 I_{th}$ , as can be seen in Figure 4.14.

The maximum single-mode power for the spatial-filtering configuration is 0.8 mW. This low power is attributed to the excessive filtering required to keep the VCSEL operating in a single spatial mode for large drive currents. Using another VCSEL from the same chip but with a 10- $\mu\text{m}$  aperture (instead of a 15- $\mu\text{m}$  aperture) maximum single mode power of 2.1 mW could be obtained. The 10- $\mu\text{m}$  VCSEL was magnified by a factor of two with the afocal imaging

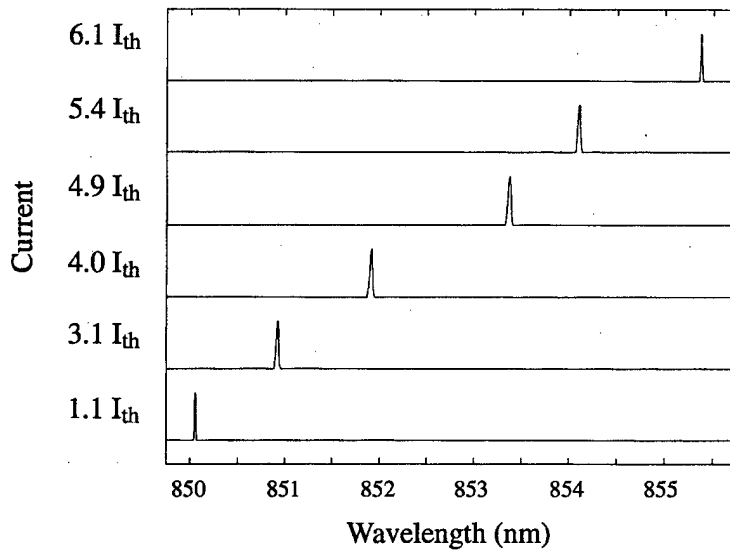


Figure 4.14. Spectral data for a 15- $\mu\text{m}$  VCSEL with spatial filtering; the VCSEL stays single mode for currents up to  $6I_{\text{th}}$ .

configuration, meaning that the imaged beam had a spot size of 20  $\mu\text{m}$ . The higher power measured is probably due to the fact that less light is being clipped by the mirror for the magnified 10- $\mu\text{m}$  device. The choice of aperture size for the micromirror might therefore be overly constrained for the 15- $\mu\text{m}$  VCSEL.

A plot of the output light intensity versus the drive current (L-I curve) for the 10- $\mu\text{m}$  VCSEL device for the two mirror locations is shown in Figure 4.15. The drop in power of the curve of the spatially-filtered VCSEL as the current is increased above 21 mA corresponds to the onset of the second-order mode. In the curve of the VCSEL without spatial-filtering the two kinks agree well with the onset of the second- and the third-order modes. Optical chaos [Chung & Lee, 1991] was also observed for some power levels and cavity adjustments of the 10- $\mu\text{m}$  device; this effect is expected from a coupled cavity configuration and would be absent in an integrated structure where the intermediate VCSEL DBR mirror stack could be removed. For the 15- $\mu\text{m}$  VCSEL optical chaos was not observed.

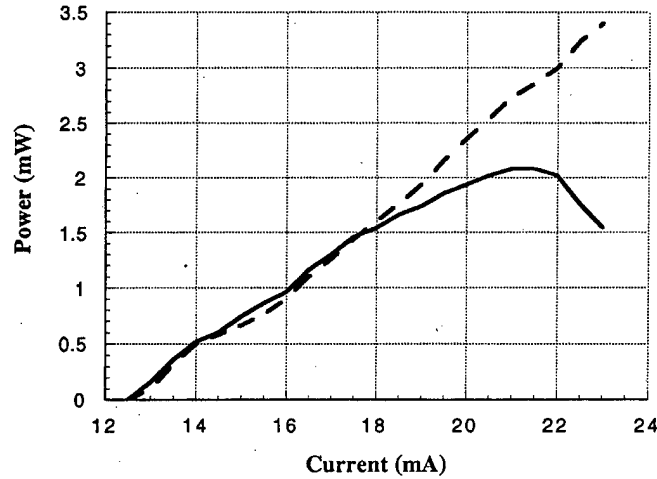


Figure 4.15. L-I curve for a 10- $\mu\text{m}$  VCSEL with spatial filtering (solid line) and without spatial filtering (dashed line).

#### 4.4.2 Replication

The mass-transport process is suitable for fabricating microoptical elements in GaP. In this particular application it is of interest to form the microstructure in GaAs. Because GaAs is used as the substrate material for VCSELs, a GaAs mirror could be directly integrated with the VCSEL, thus avoiding any refractive-index or thermal-expansion discontinuities. Some progress in GaAs mass-transport has been reported [Liau, *et al.*, 1994c]. Other groups have demonstrated the fabrication of GaAs microlens arrays by reactive ion etch transfer of reflowed photoresist [Strzelecka, *et al.*, 1997; Sankur, *et al.*, 1996] and binary diffractive optical elements fabricated in GaAs by electron-beam lithography and reactive ion beam etching [Bengtsson, *et al.*, 1996; Wendt, *et al.*, 1995].

A process has been developed for transferring a general micro-optic structure (binary or continuous relief) originally made in GaP into GaAs on the basis of replication techniques. The method is shown schematically in Figure 4.16. An original element is first manufactured by some micromachining technique (not necessarily by mass-transport). By electroformation of the master element a negative nickel (Ni) replica is produced. The Ni mold is used to replicate the surface-relief pattern into thin plastic films that are coated onto GaAs substrates. The cast pattern is finally transferred into the substrate by dry-etching techniques.

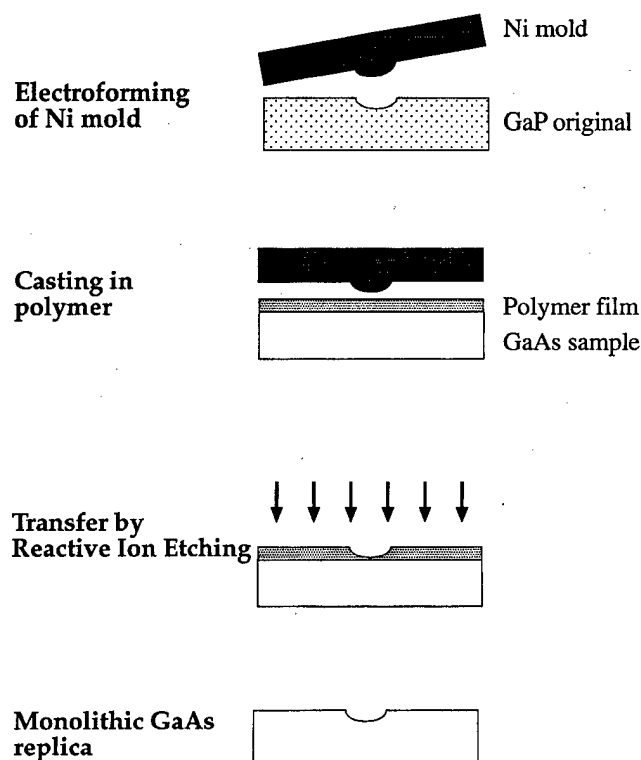


Figure 4.16. Method for replicating a microoptical structure into GaAs.

The small GaP element was glued onto a silicon substrate backing for ease of handling during the electroforming process. A 200-Å-thick Ni seed film was first sputtered over the GaP substrate to make it conductive. Next the coated GaP sample was immersed in a Ni-containing electrolyte, and a 500- $\mu\text{m}$ -thick Ni mold was obtained after plating for 20 hours. The Ni replica was separated from the master and cleaned of residual GaP. Finally, the mold was treated with a mold-release agent that covers only a few monolayers on the Ni surface.

Commercial GaAs wafers (undoped, with an orientation of  $(1\ 0\ 0) \pm 0.1^\circ$ ) were cleaved and treated with a proper silane coupling agent to enhance the adhesion between the cured polymer film and the GaAs substrate. A mixture of a commercially available Tripropylene Glycol Diacrylate (Sartomer Co., Exton, PA, Model SR 306) with approximately 1.0 wt.% of *t*-Amyl peroxy-2-ethyl-hexanoate (as a thermal initiator) was used for replicating the inverse features of the Ni mold into the thin polymer film. This particular polymer was chosen because of its good release properties and small shrinkage during curing. A small droplet of the liquid polymer was dispensed on the Ni mold, a GaAs substrate placed in contact with the mold, and a

500-g weight placed on the GaAs substrate. This procedure resulted in typical polymer film thicknesses of 3-5  $\mu\text{m}$ . The film ideally should be as thin as possible to minimize the etch-process time in the subsequent transfer into GaAs. The whole unit was cured in a convection oven heated to  $\sim 85^\circ\text{C}$  for one hour. After the curing the sample was allowed to cool to room temperature before separation. The microoptical element originally created in GaP by use of a lengthy microfabrication and mass-transport process can thus rapidly and with high fidelity be replicated repeatedly on a polymeric film that adheres to the GaAs substrate.

The cast polymeric structure was used as an erodable mask for proportional etch transfer into the GaAs substrate. Reactive ion etching (RIE) was chosen over ion beam milling because the former allows more flexible control of various etch parameters. RIE allows, for instance, the etch-rate ratio to be precisely controlled by adjusting the gas mixture in the plasma.

GaAs is typically etched in chlorine-based plasma chemistries. Especially popular are the gases chlorine ( $\text{Cl}_2$ ) and boron trichloride ( $\text{BCl}_3$ ) [Juang, *et al.*, 1994; Lee, *et al.*, 1997]. Because  $\text{BCl}_3$  is an effective getter of water vapor, and immediately attacks the native oxide layer on the GaAs surface, it is well suited for reproducible GaAs etching. However, boron and its related compounds can be deposited on the surface. These involatile products can be removed by the introduction of argon (Ar), which provides ion bombardment of the sample. The presence of Ar also aids in achieving a stable plasma and controlling the relative etch rates. Adding  $\text{Cl}_2$  further increases the GaAs etch rate. Polymeric materials (*e.g.* photoresist) are usually etched in oxygen- or fluorine-based plasmas.

Several gas mixtures of  $\text{BCl}_3$ ,  $\text{Cl}_2$ , Ar,  $\text{O}_2$ , and  $\text{CF}_4$  were investigated to obtain smooth and reproducible etching of polymeric micro-optical elements. The etching experiments were carried out by use of a Minilock RIE Etch System (Trion Technology). The samples were placed on a 6-in. silicon wafer (to eliminate backspattering of aluminum from the cathode) and introduced into the plasma reactor through a load-lock chamber. Typical etch conditions were pressures of 17-20 mTorr and a power of 100 W ( $0.55\text{ W/cm}^2$ ). To enhance the anisotropy in the etching process, one should keep the pressure low, but, because of limitations in the turbo pump capacity and gas-flow controllers lower pressures were unobtainable. Higher powers increase the etch rates (thus reducing the total etch time) but heat the polymer film so that it starts to flow.

The results demonstrate that, when even a small amount of  $O_2$  or  $CF_4$  is added to the chlorine-based gases, the etched GaAs surface is quite rough and many times covered with a black powder. Smooth GaAs etching was achieved by use of different mixtures of  $BCl_3$ ,  $Cl_2$ , and Ar. A  $BCl_3/Ar$  ratio of 1:4 resulted in etch rates of the polymer and GaAs of  $\sim 22$  nm/min. and  $\sim 40$  nm/min., respectively. A refractive biprism, fabricated by GaP mass-transport and discussed above in Section 4.2, was used as a test structure for investigating the etch process. Figure 4.17 shows a profilometer measurement of the prismatic structure cast in the polymer film. The height of the prism is  $7.3 \mu\text{m}$ . The same prism etched into GaAs is shown in Figure 4.18. The height of this etched prism is  $13.1 \mu\text{m}$ . The ratio of the two prism heights is 1.8, in good agreement with the differential etch-rate ratio. The figures show that the optical surface is well preserved during the etching process. At some locations of the etched GaAs sample small areas with narrow spikes several micrometers tall were noticed. These spikes could be removed by the addition of  $Cl_2$  to the plasma. Adding  $Cl_2$  also reduced the surface roughness of the etched GaAs

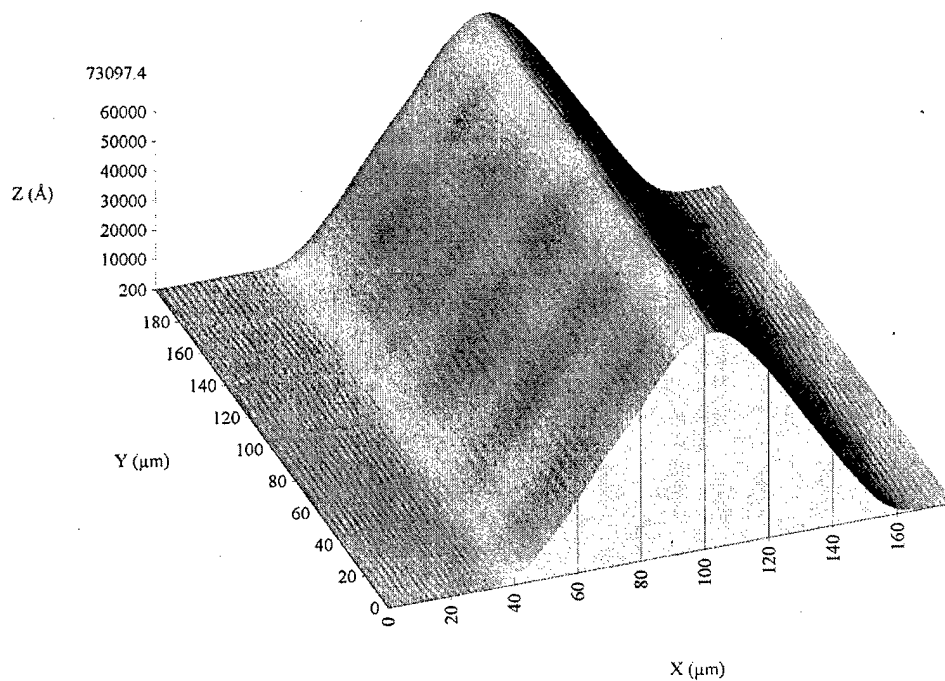


Figure 4.17. Profilometer measurement of a biprism, originally fabricated in GaP by mass-transport and subsequently cast into a thin polymer film. The height of the prism is  $7.3 \mu\text{m}$ .

samples. When  $\text{Cl}_2$  is added the etch rate of both the polymer and GaAs increases. With a  $\text{BCl}_3/\text{Cl}_2/\text{Ar}$  ratio of 1:1:4 etch rates of  $\sim 53 \text{ nm/min}$  and  $\sim 270 \text{ nm/min}$  were measured for the polymer and the GaAs, respectively. The selectivity thus increases to 5.1. As a result of the fast etch rate of GaAs in chlorine-based plasmas, it is difficult to find a gas mixture that gives an etch-rate ratio of 1:1. However, after the ratio is known it is possible to compensate for the amplification of the sag by correct adjustment of the GaP pre-form. On the other hand, the fact that the sag increases is useful because this increase permits lower aspect ratios in the mask-and-etch fabrication of the GaP mass-transport pre-form, which simplifies the pre-form generation.

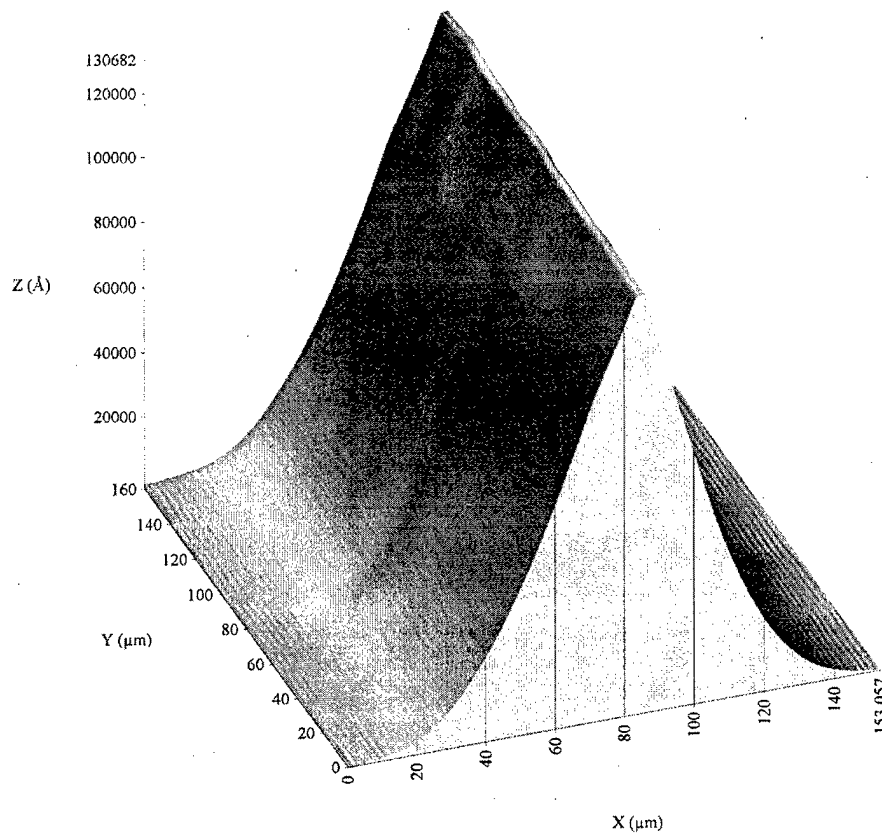


Figure 4.18. Profilometer measurement of the same biprism shown in Figure 4.17, but after transfer into GaAs. The height of the etched prism is  $13.1 \mu\text{m}$ .

After the calibration etchings, the GaP micromirror was etched. The gas mixture was a 1:1:4 combination of  $\text{BCl}_3/\text{Cl}_2/\text{Ar}$ . Figure 4.19 shows a profilometer trace measured over the center of one GaAs mirror. The sag is measured to be  $9.7 \mu\text{m}$ , which can be compared to the

original GaP mirror sag of  $1.9\ \mu\text{m}$ . A white-light interferometer was used to measure the surface profile of the mirror optically. Figure 4.20 shows an interferogram of the GaAs mirror that demonstrates an optical performance with small wave-front aberrations. The small ripple that can be seen at a few locations is believed to be caused by air trapped between the polymer and the Ni mold in the casting process, which can be avoided by further optimization of the process.

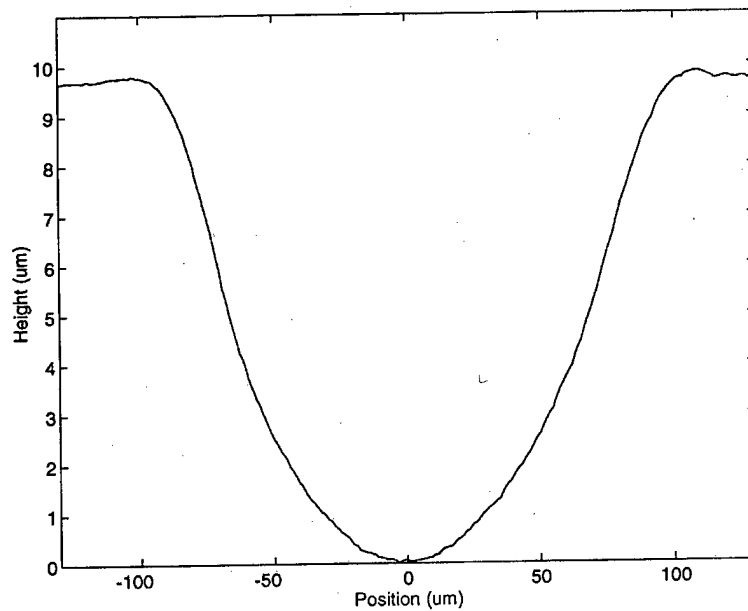


Figure 4.19. Profilometer trace through the center of a micromirror replicated in GaAs. The sag of the mirror is  $9.7\ \mu\text{m}$ .

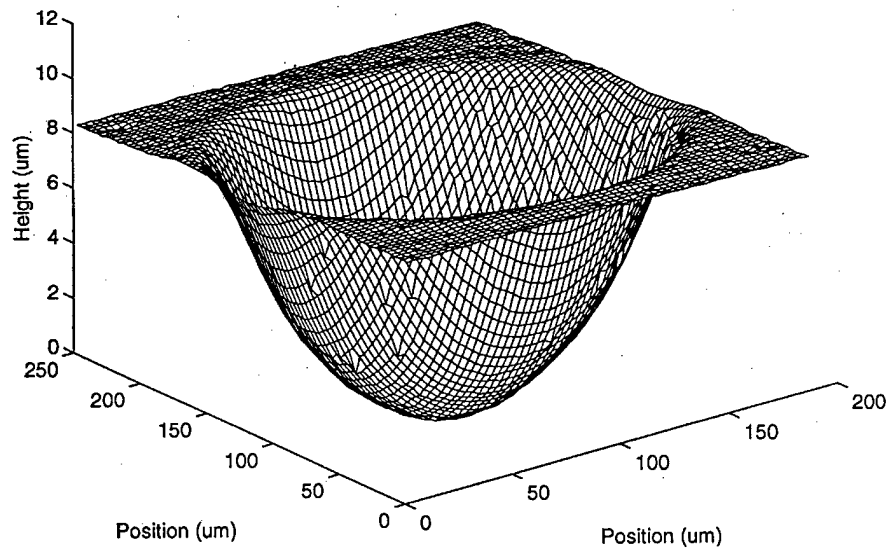


Figure 4.20. Interferogram of one replicated GaAs micromirror.

## 4.5 Vapor/Surface Diffusion

The mass-transport process is substantially different in the case where surface or vapor diffusion is the dominant transport mechanism; specifically, vapor diffusion is a faster process than surface diffusion. The relative contribution of the two diffusion mechanisms to the total transport process can be controlled by the distance between the cover wafer and the substrate surface. The mass-transport decay lifetime has either a fourth- or third-order dependence upon the spatial period of the structure, depending upon the spacing of the cover wafer. For a particular cover-wafer spacing  $s$ , there is a spatial period  $\Lambda = 2\pi s$  at which the transition between fourth- and third-order decay behavior occurs. Thus, if the cover wafer is a relatively large distance from the substrate (as compared to the spatial period of the features on the substrate) then the transport is primarily that of vapor diffusion, while if the cover wafer is closer then the transport is predominantly surface diffusion. This increase in transport speed with increased cover-wafer spacing was demonstrated (though in an approximate manner) by previous characterization experiments. While the faster speed of the vapor diffusion process is advantageous for the fabrication of optical elements, the surface diffusion process may allow more accurate control of the final surface figure. It is, therefore, useful to experimentally characterize the relationship between the two processes.

A useful method of investigating the relationship between surface and vapor diffusion is to examine the smoothing of a rough surface during mass-transport. The experimental arrangement is shown in Figure 4.21, in which a cover wafer is placed a distance  $s$  above a rough

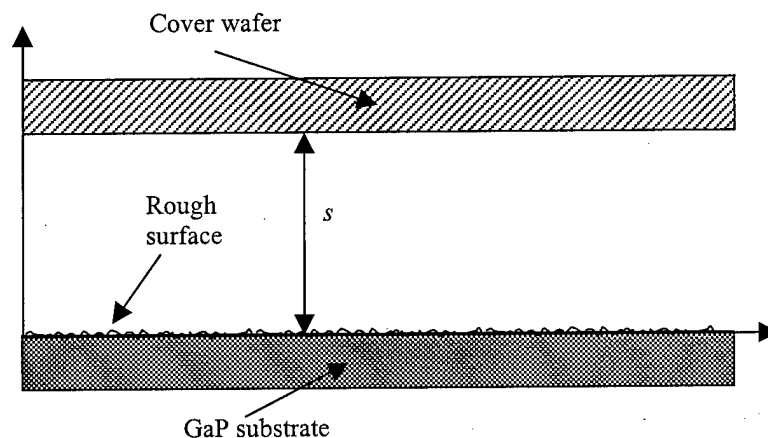


Figure 4.21. Diagram of mass-transport with cover wafer above rough GaP substrate.

GaP surface. If the statistical distribution of the roughness follows typical physical conditions, then a range of spatial frequency components are included in the roughness. Each of these components will decay exponentially in time with a lifetime that is proportional to either the third or fourth power of the spatial period, depending upon the cover-wafer spacing.

This experiment was carried out by etching trenches in a GaP substrate to a depth of 1  $\mu\text{m}$  using a rough ion-milling process. The GaP sample was cleaned using the techniques described in Chapter 3. The sapphire cover wafer was placed onto the GaP substrate; good contact between the two transparent materials was ensured by the observation of interference fringes during the evaporation of isopropyl alcohol. The GaP-sapphire sandwich was placed into a sealed ampoule and heated at a rate of 2  $^{\circ}\text{C}/\text{min}$  to  $\sim 1090$   $^{\circ}\text{C}$  followed by rapid cooling.

The surface profile was measured before and after mass-transport across a 50 x 50  $\mu\text{m}^2$  region by an AFM. The amplitudes of the Fourier coefficients of the surface roughness before and after mass-transport (averaged across the 512 rows in the data set) were then calculated from this surface data. The decay of the roughness (normalized to the data before mass-transport) is shown in Figure 4.22; the slope of this log-log plot is predicted to be either four or three for surface or vapor diffusion, respectively. For a cover-wafer spacing of 1  $\mu\text{m}$  a transition from surface diffusion (fourth power) to vapor diffusion (third power) should occur near a spatial frequency of  $1/2\pi \cong 0.16$   $\mu\text{m}^{-1}$ . As can be seen from Figure 4.22, however, the slope remains less than unity for spatial frequencies greater than 0.1  $\mu\text{m}^{-1}$ . The sub-unity (rather than third- or fourth-order) behavior of the data suggests that the mass-transport process does not follow the theoretical predictions for this experiment. It is possible that the surface passivation which terminates the mass-transport process [Swenson, *et al.*, 1995] affects the small-spatial-period components more quickly than the large-period components; thus the expected third- or fourth-order behavior is not observed.

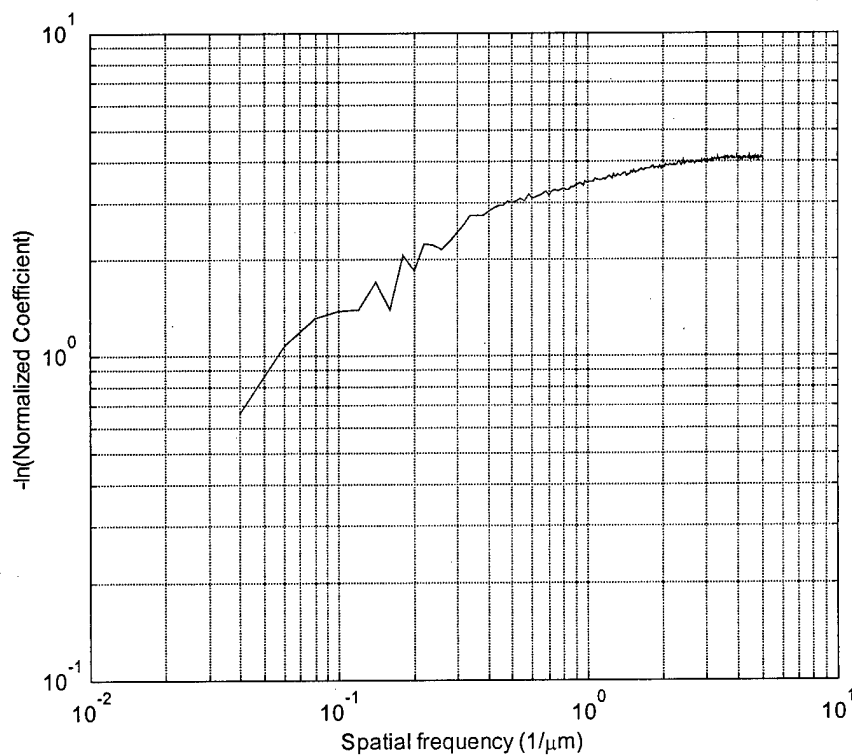


Figure 4.22. Amplitude decay of GaP surface roughness during mass-transport with 1- $\mu\text{m}$  cover-wafer spacing.

There are several possible sources of error in this experiment, including variation in cover-wafer spacing (either due to displacement during ampoule sealing or to thermal deformation) and signal-to-noise problems (caused by the small initial amplitude of the roughness and variations in wafer flatness). A more accurate measurement of the relationship between surface and vapor diffusion during mass-transport may be possible. One approach is to reduce the transport temperature in the above experiment to allow the measurement of amplitude decay before surface passivation occurs for the small-spatial-period features. Another method is to examine the decay of large-spatial-period gratings ( $\Lambda > 10 \mu\text{m}$ ) in a configuration having large cover-wafer spacing.

#### 4.6 Surface Roughness Reduction

The mass-transport smoothing process can be used to reduce the surface roughness of a micro-optical element having the correct overall surface figure. This is particularly useful if the micro-optical surface is fabricated using replication methods. Optimization of the transfer

method used to drive the original surface into the substrate (usually a dry-etch process) results in surface roughness having small amplitude and predominantly high-spatial-frequency components. The fourth-power dependence of the decay lifetime upon the spatial period shows that this roughness is quickly attenuated during the transport process. However, a much larger spatial period is associated with the entire optical surface and thus a transport time that is several orders of magnitude larger is required to significantly alter the profile. Therefore, the mass-transport smoothing process is well suited to removing roughness from an optical surface while preserving the overall (possibly aspheric) surface figure.

A polymer microlens was formed on the surface of a commercial GaP (100) substrate. This microlens was transferred into the GaP substrate by a dry-etching process to generate a GaP microlens having a diameter of 190  $\mu\text{m}$  and a sag of 25.3  $\mu\text{m}$ . Residual organic contamination from the polymer lens was removed from the substrate by use of an  $\text{O}_2$  plasma etch. To further avoid contamination from either the original polymer lens or the dry-etch transfer process the top layer ( $\sim 1.5 \mu\text{m}$ ) of the entire GaP microlens and substrate was removed in a  $\text{Cl}_2$ -based chemically-assisted ion-beam etching (CAIBE) system. The GaP substrate was cleaned and placed into a quartz ampoule following the procedures described in Section 3.5. The sealed ampoule was then placed into a tube furnace with flowing  $\text{N}_2$  and heated to 1100  $^\circ\text{C}$  for 28 hours. As discussed below, the transport time can be reduced substantially with similar effect.

The GaP microlenses were examined with a scanning-electron microscope (SEM) and an

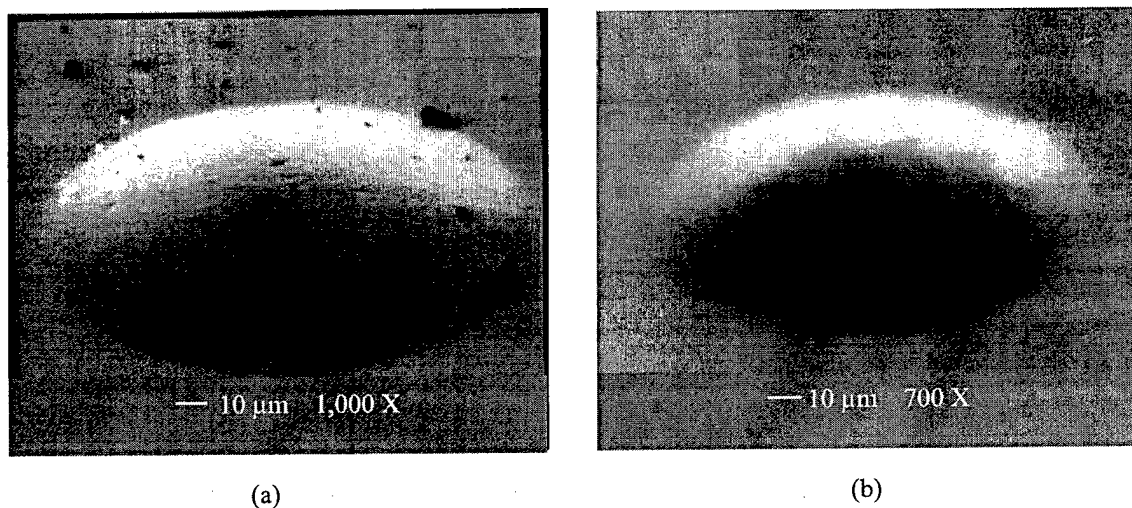
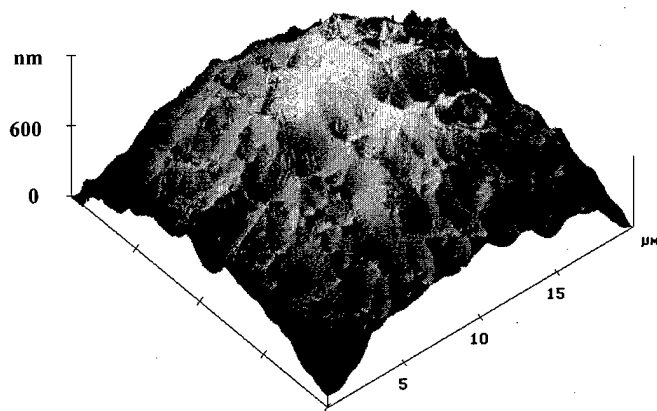
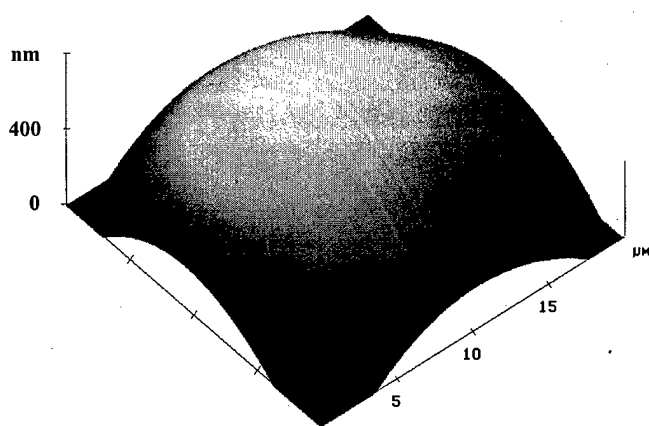


Figure 4.23. SEM image of GaP microlens (a) prior to mass-transport (b) after mass-transport.

atomic-force microscope (AFM) before and after the mass-transport process. Figures 4.23(a) and 4.23(b) show a SEM picture of a GaP microlens before and after the mass-transport process, respectively. The concentric rings on the surface of the original GaP microlens, visible in Figure 4.23(a), are removed by the mass-transport process to yield the smooth surface shown in Figure 4.23(b). AFM images of the central portion ( $20\ \mu\text{m} \times 20\ \mu\text{m}$ ) of a microlens before and after mass-transport are shown in Figures 4.24(a) and 4.24(b), respectively. The reduction of surface roughness by use of the mass-transport process can be clearly seen. Removal of linear and quadratic terms from the AFM surface profile data allows the calculation of the deviation of the GaP microlens from the desired parabolic lens shape. The surface roughness of the GaP lens was measured from the AFM data to be 50.0 nm (rms) and 6.5 nm (rms) before and after mass-transport, respectively. This reduction in surface roughness enhances the performance and efficiency of this microlens.



(a)



(b)

Figure 4.24. AFM image of GaP microlens (a) prior to mass-transport (b) after mass-transport.

A computer simulation of the mass-transport process was used to investigate the attenuation of surface roughness. A parabolic profile with identical diameter and sag ( $190\ \mu\text{m}$  and  $25.3\ \mu\text{m}$ , respectively) was used in the simulation to provide direct comparison with the experimental results described above. Mean-zero, uncorrelated, Gaussian-distributed noise with an rms of  $50.0\ \text{nm}$  was added to the surface to simulate the observed surface roughness; the resulting profile was calculated corresponding to 28 hours of mass-transport at  $1100\ ^\circ\text{C}$ . Figure 4.25 shows the difference between the final surface profile and the desired parabolic shape before (dashed) and after transport (solid). The error across 80% of the lens diameter was  $0.88\ \text{nm}$  (rms); for a simulated transport time of one hour the error was  $4.5\ \text{nm}$  (rms), roughly matching the experimentally-observed result. The mass-transport process significantly attenuated the

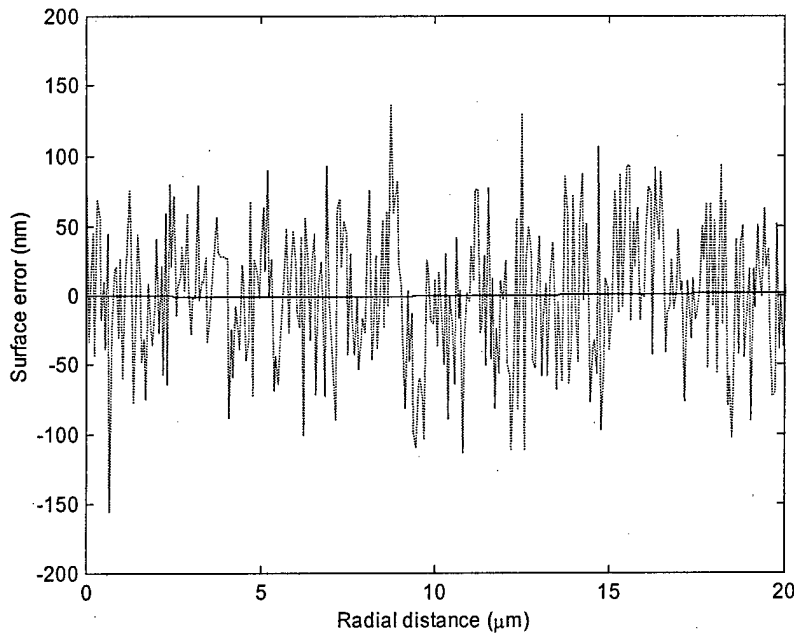


Figure 4.25. Reduction of surface roughness: deviation of surface from parabola before (dashed) and after (solid) simulated mass-transport for 28 hours.

surface roughness. To investigate the effect of the transport on the desired surface figure, a simulated mass-transport of the original parabolic surface profile (without random noise) was performed. Figure 4.26 shows the difference between the parabolic surface figure following mass-transport and the desired parabolic surface for transport times of 1 (solid), 10 (dashed), and 28 hours (dot-dash). Surface errors occur at the lens perimeter as a result of the decay of high spatial-frequency components from the edge discontinuity; these errors grow and propagate inward with increasing transport time. In each case, however, the surface profile near the center of the lens is unaffected. Therefore, a short transport time (~1 hour) is sufficient to eliminate the majority of the roughness surface across a significant portion of the lens diameter (e.g. 80%) without altering the surface figure.

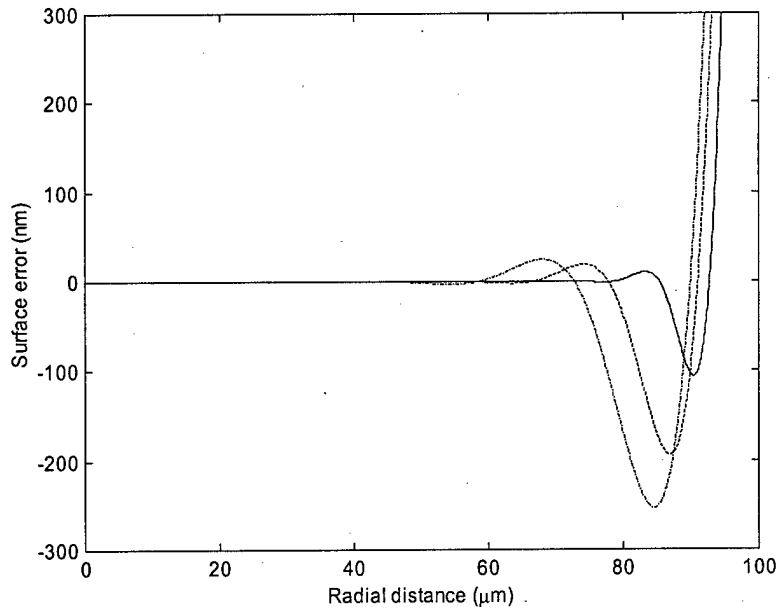


Figure 4.26. Preservation of surface figure: deviation of surface from parabola following simulated mass-transport for 1 (solid), 10 (dashed), and 28 hours (dot-dash).

#### 4.7 Effects of Pre-Form Etching Errors

There are several types of errors that can occur during the etching of a binary preform, and each has a different effect on the final surface after mass-transport. A uniform error in etch depth results in a multiplicative error of the profile height across the lens surface; the final height at a particular location is the design height multiplied by the ratio of the actual etch depth to the design etch depth. For the case of a spherical lens the surface becomes aspheric; however, for small etch-depth errors the departure from a spherical surface is negligible. Thus, small etch-depth errors change the radius of curvature of a spherical lens, with a corresponding shift in focal length. Uniform undercutting of each mesa, however, subtracts the same mass from each mesa. As mass is conserved during mass-transport, this means that the change in mass (hence in height difference) between neighboring pixels after mass-transport remains unaltered with uniform pre-form undercutting. Thus uniform undercutting acts as a piston term that reduces the sag of the element while leaving the surface figure in the central region of the lens unaltered. The surface figure near the element perimeter changes, however, as a result of the change in the substrate's flatness level. Finally, nonuniform undercutting errors are possible, such as aspect-ratio-dependent undercutting. As the partial pressure of the reactant gas can vary with the trench aspect ratio, scattering collisions between incoming neutral atoms from the beam and the reactant molecules lead to sidewall bombardment that varies with the mesa fill factor. Also, because the

desorption of  $\text{GaCl}_3$  is enhanced at elevated temperature, spontaneous chemical etching of the GaP by the  $\text{Cl}_2$  gas increases with substrate temperature. Thus, if improper heat sinking of the GaP is present, a rising substrate temperature during etching will lead to progressively greater undercutting. These substrate-temperature effects have been studied previously for several materials of interest [Grande, *et al.*, 1990; Youtsey, *et al.*, 1994]; the exact type of undercutting is usually system dependent and needs to be measured for each machine. Once known, this undercutting can be compensated in the design of the pre-form.

In addition to errors caused by undercutting in the etching process there are several other sources of fabrication error that influence the shape of the pre-form. Linewidth errors in either the mask fabrication process or the photolithography step are usually constant and result in a uniform mesa width error. This constant width error creates the piston term described above in conjunction with uniform undercutting. A more serious error arises from the aspect-ratio dependence of the substrate etch rate. The variation in partial pressure of the reactive gas above the substrate surface in the vicinity of trenches causes the etch rate to be lower in trenches that are narrow and deep as compared to trenches that are shallow and wide. The most difficult aspect of compensating for this type of error is that the etch rate difference is negligible at the beginning of etching, but becomes increasingly significant during the later stages of etching a deep structure. All of these fabrication errors contribute to the total pre-form error; it is the net effect of these errors that is measured and requires compensation.

In the experimental mass-transport examples described above (Sections 4.3 and 4.4) little error that is attributable to non-uniform pre-form fabrication errors was observed in the final surfaces. The sag of the off-axis lens and concave mirror in these cases, however, was relatively small ( $\sim 4$  and  $2 \mu\text{m}$ , respectively). The small vertical height of these structures obscures the subtle nature of pre-form fabrication errors. These errors become more noticeable when optical elements with larger sag are fabricated. To generate high-quality surfaces that match the desired surface figure it is necessary to measure the pre-form fabrication errors and compensate the design accordingly.

The fabrication errors present in a one-dimensional binary pre-form can be determined experimentally by etching a series of one-dimensional gratings having a constant period but different fill-factor. If the grating period is made small enough relative to the "diffusion length" the mass-transport process causes the gratings to completely smooth out. This creates a flat region

whose height above the original etched surface is determined by the effective pre-form grating fill-factor (which includes all fabrication errors, including mask line-width errors, imprecise exposure and development during photolithography, and undercutting in the etching process). Thus a calibration curve can be created that plots the effective fill-factor achieved following mass-transport as a function of the designed fill-factor present on the mask.

The cumulative effect of fabrication errors was measured for some etch-depths of interest using gratings having a 12.5- $\mu\text{m}$  period and fill-factors ranging from 10% to 90%. Two separate GaP samples were patterned with photoresist and etched to depths of 17.6 and 26.8  $\mu\text{m}$ , respectively. As a result of the limited differential-etch ratio a thick layer of photoresist ( $\sim 2 \mu\text{m}$ ) was required for both etches. The thick photoresist did not allow good resolution of the 10% and 90% grating lines; these data points are therefore suspect. After etching, the samples were sealed into separate ampoules and heated at 1100  $^{\circ}\text{C}$  for 28 hours. The height of each grating above the original etched surface was measured using a stylus profilometer; from these data the effective fill-factors were calculated. A plot of the data is shown in Figure 4.27, where the dashed line

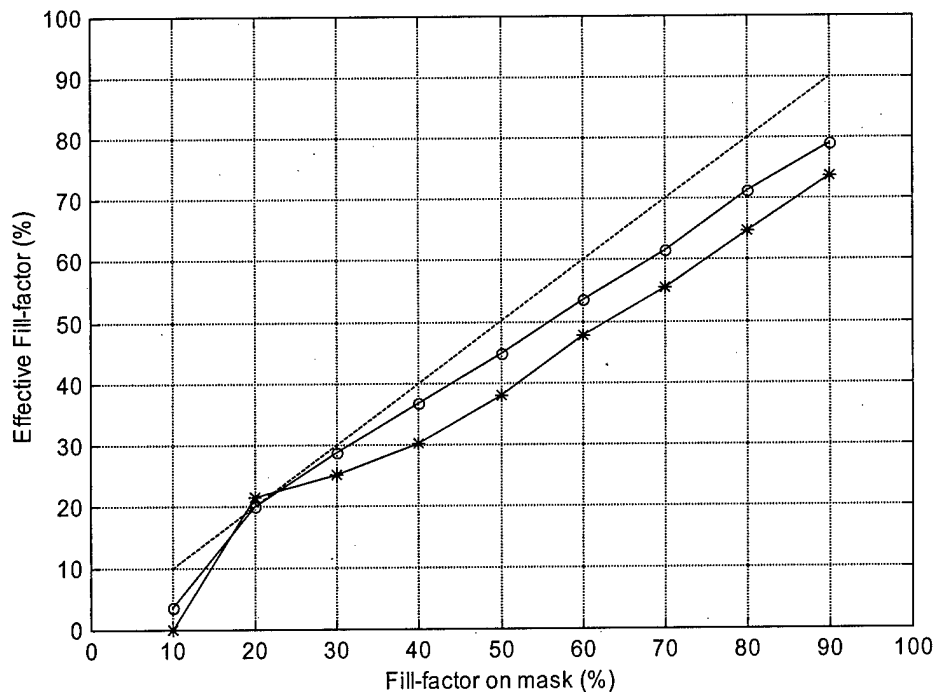


Figure 4.27. Calibration plot of effective fill-factor vs. mask fill-factor: ideal case (dashed line), 17.6  $\mu\text{m}$  etch depth (o), 26.8  $\mu\text{m}$  etch depth (\*).

shows the ideal case (no reduction in effective width of features), the line with open circles (o) shows the 17.6  $\mu\text{m}$  etch-depth data, and the asterisks (\*) shows the 26.8  $\mu\text{m}$  etch-depth data. The shallower depth data is nearly linear while the deep-etch data shows a small amount of super-linearity. Interestingly, both sets of experimental data show nearly ideal behavior for a 20% fill-factor. As expected, the 10% fill-factor data points for both curves do not lie along a smooth line connecting the rest of the data and thus represent an unusable fill-factor. However, the 90% fill-factor points agree well with the other data, suggesting that the nature of the fabrication errors allow the use of this end of the fill-factor range. The useable fill-factor range for these etch-depths is therefore reduced to 20-79% for the 17.6- $\mu\text{m}$  depth and 20-74% for the 26.8- $\mu\text{m}$  depth. These calibration curves have been used to compensate the design of the optical elements described in Section 4.8.

#### **4.8 Optical Interconnection**

Technological advances continue to reduce the size of individual electronic logic circuits through a reduction in the minimum feature size of integrated circuit components. At the same time, the total chip area continues to increase. The continued shrinking of circuit size and increase of chip area in electronic integrated circuit technology places increasing demands upon the ability to provide connection both between circuits on the chip and especially between chips. While the number of logic circuits of a particular size is directly proportional to the total chip area, the space available for interconnection grows only as the square-root of the chip area. This disparity is the result of the planar nature of integrated-circuit technology which limits connection sites to the chip edge. It has therefore been proposed to use optical methods to interconnect chips to alleviate the problem of high electronic interconnection density at the chip edge by use of the third available spatial dimension. Some of the issues involved in the optical interconnection of electronics include the identification of applications requiring high data-transfer capacity, improvement in opto-electronic device performance, and development of low-cost packaging systems that conform to the required alignment tolerance [Tooley, 1996].

For the typical case of a uniform VCSEL array on a rectangular grid, the simplest form of optical interconnection is a direct relay/imaging onto a detector array with identical pitch. A variety of imaging systems can be used to accomplish this relaying task; however, the simplest possible imaging system is a single lens with focal length chosen to provide 1:1 imaging. The single lens minimizes the size and optomechanical complexity of the imaging system. The system that accomplishes this interconnection task is shown in Figure 4.28, where a microlens array has been used to collimate the light emerging from each VCSEL; the dotted lines represent collimated beams. The singlet (used in a  $4f$  configuration) images the collimating microlens array onto the focusing microlens array. As can be seen, the clear aperture of the large imaging singlet must be larger than the VCSEL array to capture all beams. Large VCSEL and detector arrays require a large imaging lens and thus increase the bulk and cost of the system. Of greater significance, however, is the distortion present in such an optical design. The distortion is shown in Figure 4.28 by the beams which begin at an intermediate off-axis position (second from top and second from bottom) of the VCSEL array and (after passing through the imaging singlet) do not strike the center of the corresponding microlens used to concentrate light onto the detector array. At the edge of the VCSEL array the beams completely miss their corresponding microlenses, thus causing either loss of a channel or cross-talk between channels. This distortion is clearly unacceptable in an optical interconnect system and requires correction.

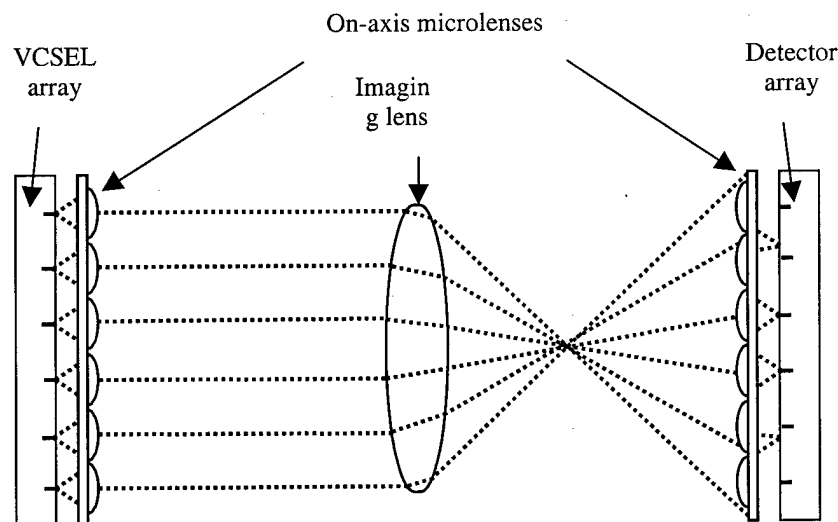


Figure 4.28. Optical interconnect system exhibiting distortion.

It has recently been shown that it is possible to eliminate distortion in a multi-chip optical interconnect system on a self-similar grid arrangement by appropriate placement of the system aperture to create a symmetric optical system [Christiansen, *et al.*, 1999]. This correction is accomplished by the introduction of prismatic elements that steer beams from small-divergence sources through the center of a relay lens; extension to a rectangular grid arrangement allows implementation with single-chip interconnection systems.

A diagram of the design modified for use with a rectangular grid arrangement is shown in Figure 4.29. The array of off-axis microlenses collimates each of the VCSELs and steers the beams through the center of the imaging lens. The large singlet images the off-axis collimating microlens plane onto the focusing microlens plane (which concentrates the light onto the small-area detectors). (The focusing microlens array can be eliminated if large-area detectors are used.) As can be seen by a comparison of Figures 4.28 and 4.29, a smaller portion of the singlet is illuminated when the beams are steered, thus decreasing the size of the lens needed for the imaging system. Steering the beams through the center of the imaging lens also moves the effective aperture stop to the center of the imaging lens and creates a symmetric optical system. Symmetric optical systems have the desirable quality that three aberrations – coma, distortion, and transverse chromatic aberration – are eliminated.

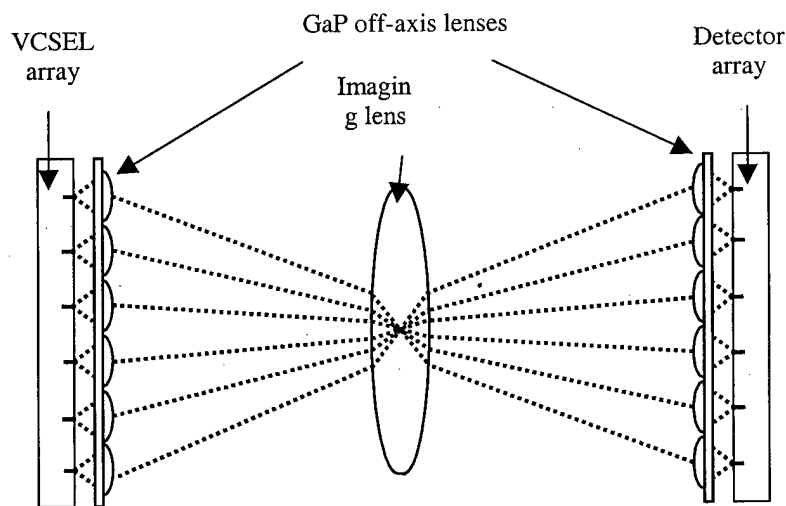


Figure 4.29. Diagram of optical interconnect system using off-axis GaP microlenses for distortion elimination.

The system is designed to incorporate a 9 x 9 square array of small-aperture VCSELs (half-angle divergence  $\sim 15^\circ$ ) with 500- $\mu\text{m}$  pitch operating at a wavelength of 850 nm. The VCSELs are collimated by microlenses having a diameter of 150  $\mu\text{m}$ . During propagation these collimated beams will experience nominal far-field divergence of  $\sim 0.3^\circ$  as a result of the microlens aperture size. Each collimated VCSEL beam can thus be accurately modeled using geometric optics as a small patch of point sources, each emitting with a  $0.3^\circ$  half-angle. The focal length of the imaging singlet is chosen to be 10 mm; a 1:1, 4- $f$  imaging configuration results in object and image distances of 20 mm. (In practice, the 10-mm symmetric-convex lens is replaced by two plano-convex lenses each having a 20-mm focal length; the purpose of this substitution is discussed at the end of this section.)

Modeling of the optical design using a commercial ray-tracing optical design program (Code V<sup>TM</sup>) allows quantification of the improvement possible by use of off-axis collimating lenses. Figure 4.30 shows a Code V system diagram for the case where the collimated beams are not steered. Rays are traced for three object field points; the farthest off-axis location is 2.828 mm, corresponding to the corner element of the 9 x 9 VCSEL array. A plot of distortion as a

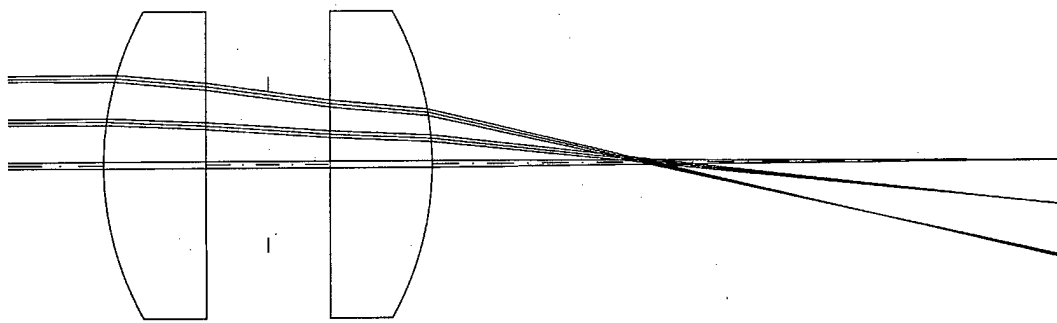


Figure 4.30. Code V system diagram showing three object field points; beams emit perpendicular to VCSEL substrate.

function of fractional object height (shown in Figure 4.31) shows that the distortion reaches  $\sim 11\%$  at the array corner. This amount of “pincushion” distortion would cause significant problems when used in conjunction with a square array of detectors. Incorporation of the beam-steering microlenses results in the system diagram shown in Figure 4.32. All rays cross the optical axis at the center of the optical system. The object and image distances are equal (for 1:1

imaging) and have been optimized for the on-axis field point. An optical-path-difference (OPD) calculation for the system depicted in Figure 4.32 is shown in Figure 4.33; all field locations exhibit an OPD  $< \lambda/100$  with respect to the curved image plane. Although distortion is eliminated in this configuration, significant curvature-of-field is present. However, the imaging system is operating at small numerical-aperture and thus has a large depth-of-focus; the effect of the curvature-of-field on the optical performance of this system is therefore considered negligible.

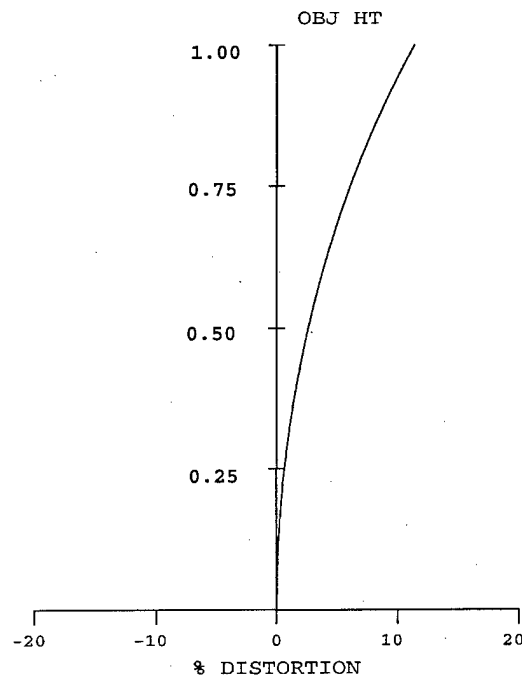


Figure 4.31. Plot of distortion as a function of fractional object height (1.0 object height corresponds to 2.828 mm) for system shown in Figure 4.30.

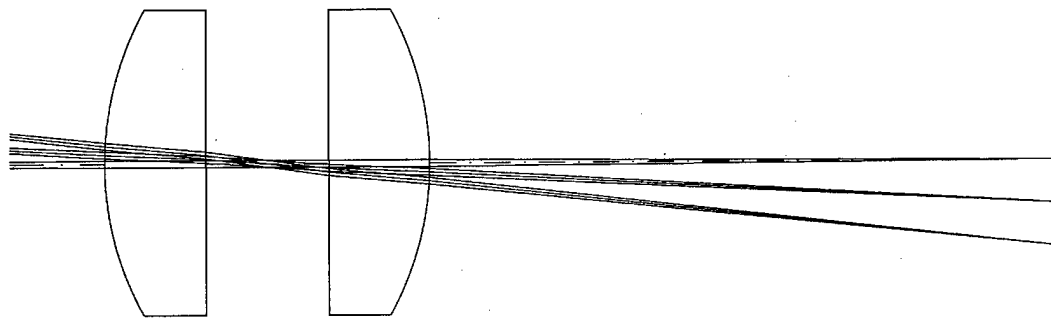


Figure 4.32. Code V system diagram showing three object field points; beams steered through center of imaging system.

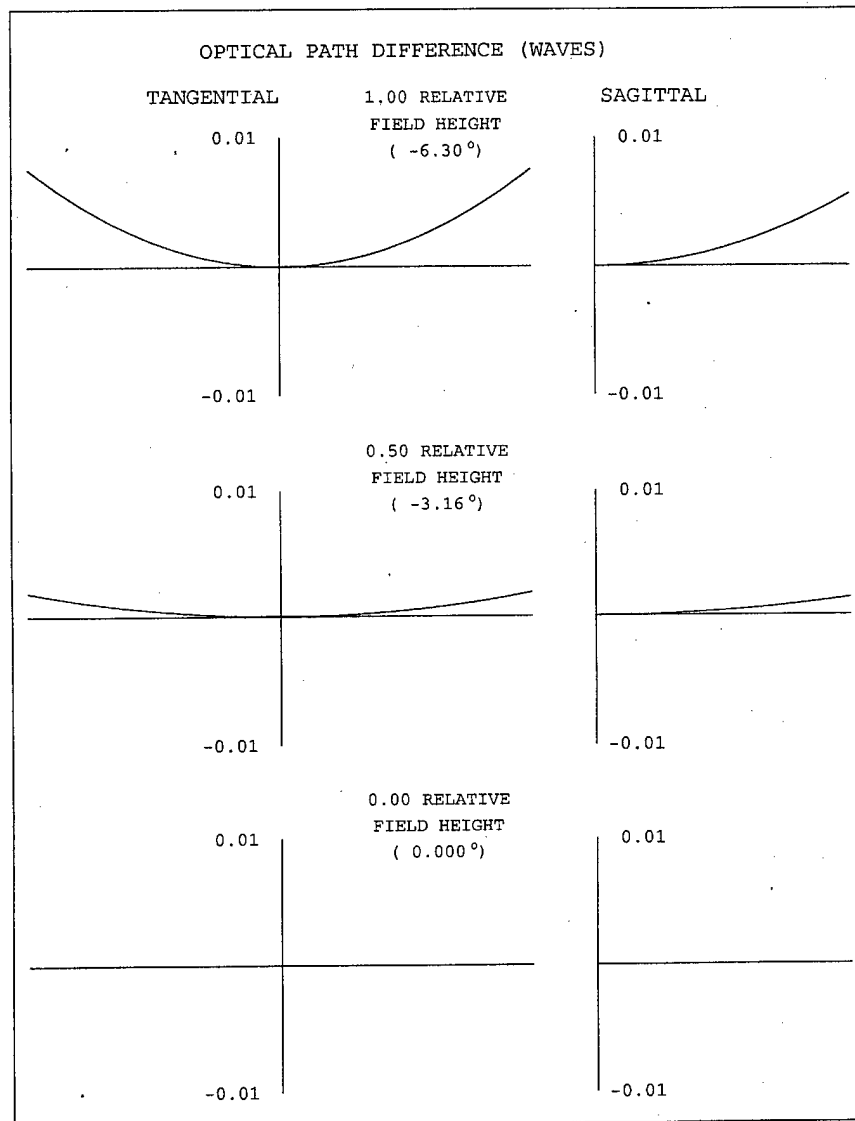


Figure 4.33. OPD calculation for steered beams (three object field points).

The off-axis GaP microlens surfaces needed to collimate and steer the individual VCSEL beams were designed using Code V<sup>TM</sup>. Each design surface was optimized as a fourth-order polynomial in rectangular coordinates and had an OPD of  $\sim \lambda/100$ . These surfaces were used to generate a one-dimensional mesa-width modulation mask pattern (discussed in Section 2.2.2); the pre-form calibration data described in Section 4.7 were used to compensate the design for

expected fabrication errors. The pre-form was generated in the surface of a GaP substrate following the fabrication steps described in Chapter 3. After cleaning, the GaP pre-form was placed into a sealed ampoule and heated at 1100 °C for 30 hours; a second 30-hour transport time was used to remove small ripples resulting from incomplete smoothing.

Measurement of the resulting GaP microlenses by the use of a stylus profilometer revealed errors in the fabricated surface profiles. An etch-depth error ( $\sim 0.3 \mu\text{m}$  too shallow) and a change in the nature of undercutting during etching (discussed in Section 4.7) adversely affected the surface profile. In the original design each GaP microlens could be approximated by a spherical surface with 545- $\mu\text{m}$  radius-of-curvature (shifted by an appropriate amount to give off-axis beam-steering). As a result of the fabrication errors, the radius-of-curvature of the best-fit spherical surface for each lens increased by 7-14%, with the lower and upper ends of the range corresponding to the on-axis and farthest off-axis lenses, respectively. (A constant error in lens focal length causes errors in the steering angle for the off-axis lenses; non-uniformity of focal length introduces errors in beam collimation for a fixed microlens array working distance.) The farthest off-axis lens had a deviation of  $\sim \lambda/13$  (rms) from a best-fit spherical surface, resulting in a calculated Strehl ratio of  $\sim 77\%$ .

The distortion (present in the optical interconnect system without the addition of beam-steering micro-optics) was verified by the placement of an aperture mask (consisting of a 9 x 9 array of 200- $\mu\text{m}$  diameter clear apertures with a pitch of 500  $\mu\text{m}$ ) in the object plane of the optical system. Illumination of the apertures by a plane-wave simulates an array of VCSELs collimated by on-axis lenses (as shown in Figure 4.28). An image of the intensity at the image plane of the interconnection system for this situation is shown in Figure 4.34. The distortion is clearly evident at the corners of the array; a grid of lines has been overlaid on the intensity data to emphasize the distortion. A distortion of 11.0% was measured for the corner element of the array; this agrees well with the design value shown in Figure 4.31 (11.3%). The array of GaP microlenses was then placed in the object plane of the interconnect system. A one-dimensional VCSEL array containing five lasers was used to illuminate five microlenses. Translation of the VCSEL array (while the microlens array and image plane remain stationary) allowed testing of all lenses in the array. Superposition of the resulting images allows the creation of the image shown in Figure 4.35 (where a grid of lines has been overlaid on the intensity data); the distortion has been eliminated through the use of the GaP beam-steering microlenses.

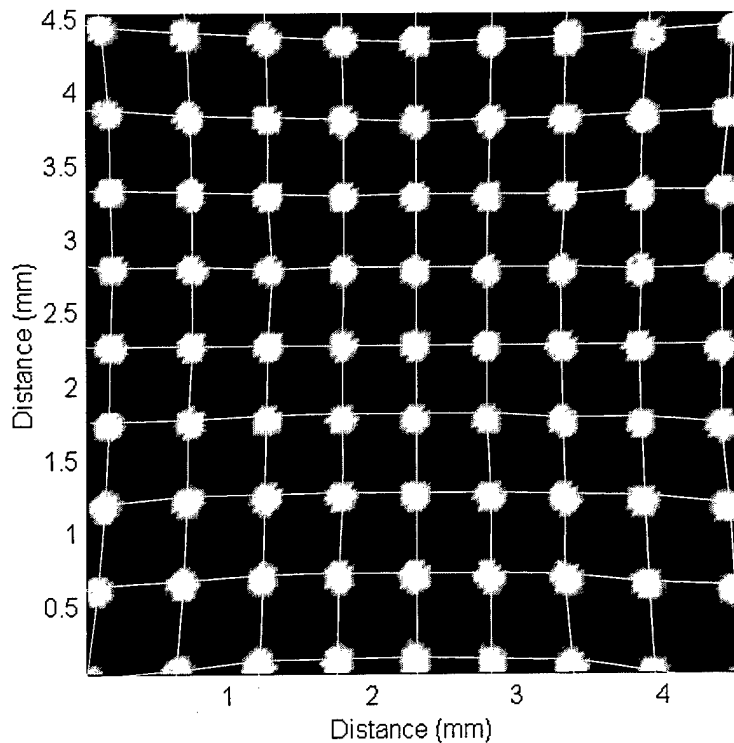


Figure 4.34. Image of clear aperture array through imaging system; simulation of distortion shown in system of Figure 4.28.

A microscope objective was used to form a point source that was collimated by the on-axis microlens. The divergence of the collimated beam from the on-axis microlens was measured to be approximately 1.5 times the diffraction limit from an aperture with a diameter of  $140\ \mu\text{m}$  (the size of the illuminated portion of the microlens). This increase in divergence is the result of aberrations induced by the errors in the microlens profiles; these profile errors were caused by the non-ideal pre-form etching characteristics discussed above. These aberrations also reduce the fraction of energy contained within the central lobe of the Airy pattern transmitted by each lens; the central lobe of the on-axis lens contains 45% of the total power (as compared to a theoretical value of  $\sim 84\%$  [Born & Wolf, 1980]). The error in microlens surface figure has also introduced errors in the angle through which each beam is steered. The lens at the center of one edge of the array (having an off-axis position of 2 mm) was designed to steer the collimated VCSEL beam by an angle of  $4.1^\circ$ ; the actual steering angle was measured to be  $3.8^\circ$ . However, the majority of the total energy ( $>90\%$ ) within the central lobe of the Airy-disk pattern transmitted by each microlens is contained within a circle of diameter 1 mm at the aperture of the

image-relay lenses. Therefore, the small errors in beam-steering do not seriously compromise the symmetry of the optical system or increase the aberrations.

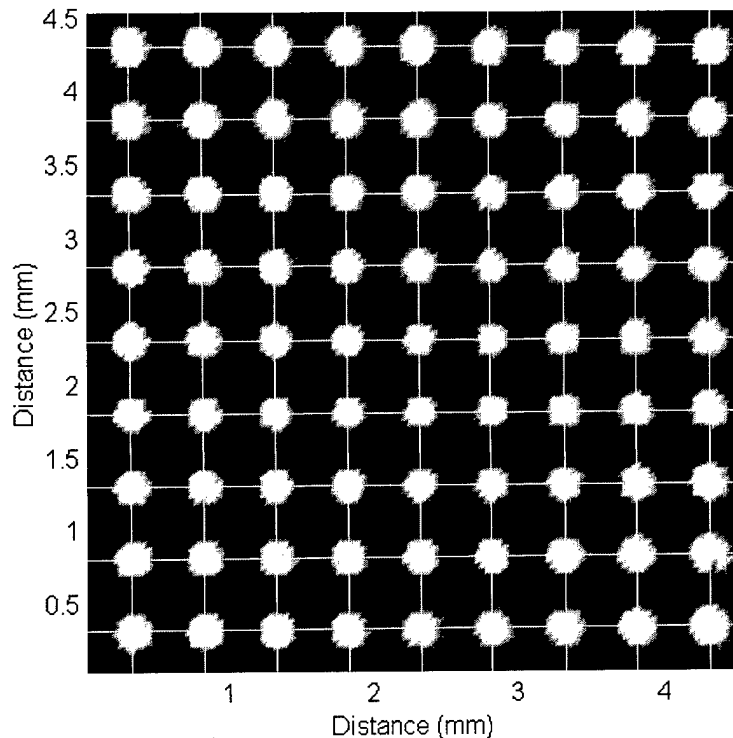


Figure 4.35. Image of VCSEL array incorporating beam-steering microlenses; distortion eliminated.

An interconnection technique similar to the one discussed here has been described in which both the microlens and image-relay lens are fabricated using diffractive optics [Morrison & Buchholz, 1998]. The single image-relay lens described earlier in this section has been replaced in this demonstration by an array of image-relay lenses that only allow for local interconnections. This substitution is necessary to avoid one of the fundamental disadvantages of diffractive optics: it is difficult to fabricate high-efficiency diffractive lenses designed to operate either at small  $f/\#$  or with object points located far off-axis. For that reason, the above diffractive-optics demonstration employed modest  $f/\#s$  and steering angles for the microlens and image-relay lens arrays. While the GaP microlenses fabricated by mass-transport and described earlier in this section also operate with relatively small steering angles ( $\theta_{\max} \cong 6.3^\circ$ ), the steering angle can be increased without loss of efficiency through the use of a multi-level mass-transport

pre-form or through improvement of the single-etch pre-form process. This increase in steering angle allows communication between data channels on opposite corners of the array. The diffractive optics demonstration, on the other hand, divides the VCSEL array into regions covered by each image-relay lens; communication is not allowed between channels covered by different image-relay lenses. Also, the work using diffractive optics demonstrates chromatic insensitivity to wavelength changes of  $\pm 10\%$ . However, this tolerance depends upon the  $f/\#$ s and relative focal lengths of the lenses used in the interconnection system. Therefore, depending upon the array dimensions, interconnection distance, source wavelength range, *etc.*, a refractive solution may be preferable.

Another interconnection system employing both macro- and micro-optics that is very similar to the work described in this section has been described using diffractive optics in a planar optics configuration [Sinzinger & Jahns, 1997]. This demonstration employs a single image-relay lens of small size that acts as a field lens between two microlens arrays. One microlens array forms images of the input channels at the plane of the relay lens; each microlens provides off-axis steering to form superimposed images at the relay-lens plane. The second microlens array forms images at the output plane. One disadvantage inherent in this approach is the need to form an image at the relay-lens plane; the microlens quality needs to be higher for use in an imaging configuration than for use to reduce the divergence of each channel to allow the image-relay lens to operate at small numerical-aperture. In addition, the microlenses and image-relay lens in this demonstration were implemented as diffractive lenses having efficiencies of 40% and 81%, respectively. Replacing these elements with refractive surfaces provides substantial improvement to the system power budget.

Although distortion-free imaging of an extended object field can be accomplished by other optical systems using multiple elements (*e.g.* photolithography systems), the design used in this demonstration has the advantage of employing a single image-relay lens (used at a small numerical aperture) in conjunction with a compact microlens array. The entire design contains a small number of components and can be easily integrated into a modular structure. In addition, the small diameter and spherical form of the image-relay lens suggests that it can be fabricated as a "large" microlens using some simple micro-optical fabrication techniques (*e.g.* photoresist reflow) and integrated using silicon micro-bench techniques [King, *et al.*, 1996]. As this experiment has demonstrated, this design is tolerant to misalignment (errors in beam-steering

angle did not impact performance) and to aberrations induced by the microlens array. This design tolerance is the result of the image-relay lens providing the imaging characteristics of the system, while the microlens array reduces the VCSEL divergence to make the image-relay system operate at a small numerical aperture and directs the light in the appropriate direction to eliminate distortion. Furthermore, this design is physically symmetric, meaning that the system can be folded in half (making the object and image planes coincident) through the placement of a mirror at the effective system aperture stop. An appropriate tilt of this mirror allows the interlacing of the object and image points and the application to a system using a "smart-pixel" array.

## 5. Conclusions

Gallium-phosphide refractive micro-optical elements have been fabricated by mass-transport smoothing. This technique allows the fabrication of optical elements with low  $f/\#$  and aspheric surface figure directly in a material with high refractive index, resulting in increased design freedom in optical systems.

An approximation to the desired optical surface (the pre-form) is fabricated in a gallium-phosphide substrate using anisotropic etching techniques. The pre-form is then smoothed into the final surface by the mass-transport process, in which surface-energy minimization drives material diffusion at elevated temperature in a sealed ampoule. A favorable variation of smoothing with the spatial period of the surface-relief structure allows the quick smoothing of the sharp edges of the pre-form while preserving the overall shape of the optical element, thus allowing good control over the final surface figure.

Refractive gallium-phosphide micro-optical elements are demonstrated using single- and multi-step pre-forms, including a Fresnel biprism and an off-axis aspheric collimating lens. New pre-form designs with relaxed fabrication tolerance are also introduced. A concave mirror is fabricated and used for spatial-mode control of a vertical-cavity surface-emitting laser (VCSEL). This concave mirror has also been replicated into a GaAs substrate by a casting and dry-etch transfer process. The effect of the spacing of a sapphire cover-wafer above the gallium-phosphide substrate during mass-transport is investigated to test theoretical predictions of the relationship

between surface and vapor diffusion. An array of off-axis lenses is fabricated and integrated with an array of VCSELs to eliminate distortion in an optical interconnect system.

Mass-transport is capable of generating very smooth surfaces as a result of the material diffusion process. The surface height is quantized only to the extent that the pre-form fabrication process has finite resolution; use of an electron-beam photomask and high-performance lithography and etching techniques allow accurate control of pre-form characteristics. It is also the only technique capable of generating arbitrary surface profiles of significant height (sag > 10  $\mu\text{m}$ ) directly in a semiconductor substrate. As a result of the smoothing of small horizontal features it is difficult to make structures that have vertical sidewalls after mass-transport. Therefore, while mass-transport is a good technique for making refractive surfaces, it is an inappropriate choice for making diffractive optical elements.

## 6. List of Publications

- Ballen, T.A. and Leger, J.R. (1998) "Mass-transport gallium-phosphide refractive micro-lenses for diode array reconfiguration," in *Diffractive Optics and Micro-Optics*, Vol. 10, OSA Technical Digest Series, 186-188.
- Ballen, T.A. and Leger, J.R. (1999) "Mass-transport fabrication of off-axis and prismatic gallium phosphide optics," *Appl. Opt.* **38**, 2979-2985.
- Nikolajeff, F., Ballen, T.A., Leger, J.R., Gopinath, A., Lee, T.-C. and Williams, R.C (1999) "Spatial-mode control of vertical-cavity lasers with micromirrors fabricated and replicated in semiconductor materials," *Appl. Opt.* **38**, 3030-3038.
- Nikolajeff, F., Ballen, T.A., Leger, J.R., Gopinath, A., Lee, T.C. and Williams, R.C. "Mass-transported micromirror for mode control of vertical cavity laser," *Conf. on Lasers and Electrooptics (CLEO)*, Baltimore, MD (1999).
- Nikolajeff, F., Leger, J.R. and Ballen, T.A. "Micro-optical elements fabricated and replicated in semiconductor materials," *SPIE Photonics West '99 Technical Digest*, San Jose (1999).
- Ballen, T.A., Leger, J.R., Glumac, D.E., Swanson, L.S. and Gage, E. "Use of mass-transport to reduce surface roughness in replicated gallium-phosphide refractive microlenses," submitted to *Optics Letters*.
- Ballen, T.A. and Leger, J.R. "Use of refractive mass-transported off-axis gallium-phosphide

micro-optics in a distortion-free optical interconnection system," in preparation.

## 7. List of Participating Scientific Personnel & Advanced Degrees Earned

James R. Leger, Professor, Department of Electrical and Computer Engineering

Todd A. Ballen, Research Assistant; M.S.E.E. earned Jan. 1998, Ph.D. earned Dec. 1999.

Fredrik Nikolajeff, Postdoctoral Research Associate

## 8. Bibliography

- Ballen, T.A. and Leger, J.R. (1998) "Mass-transport gallium-phosphide refractive micro-lenses for diode array reconfiguration," in *Diffraction Optics and Micro-Optics*, Vol. 10, OSA Technical Digest Series, 186-188.
- Ballen, T.A. and Leger, J.R. (1999) "Mass-transport fabrication of off-axis and prismatic gallium phosphide optics," *Appl. Opt.* **38**, 2979-2985.
- Bengtsson, J., Eriksson, N. and Larsson, A. (1996). "Small-feature-size fan-out kinoform etched in GaAs," *Appl. Opt.* **35**, 801-806.
- Born, M. and Wolf, E. (1980) *Principles of Optics: Electromagnetic Theory of Propagation, Interference and Diffraction of Light*, (Oxford: Pergamon), p. 398.
- Campbell, S.A. (1996) *The Science and Engineering of Microelectronic Fabrication*, (Oxford: Oxford UP).
- Chen, G., Leger, J.R. and Gopinath, A. (1999) "Angular filtering of spatial modes in a vertical-cavity surface-emitting laser by a Fabry-Perot etalon," *Appl. Phys. Lett.* **74**, 1069-1071.
- Christensen, M.P., Milojkovic, P. and Haney, M.W. (1999) "Low-distortion hybrid optical shuffle concept," *Opt. Lett.* **24**, 169-171.
- Chung, Y.C. and Lee, Y.H. (1991) "Spectral characteristics of vertical-cavity surface-emitting lasers with external optical feedback," *IEEE Photonics Technol. Lett.* **3**, 597-599.
- Grande, W.J., Johnson, J.E. and Tang, C.L. (1990) "Characterization of etch rate and anisotropy in the temperature-controlled chemically assisted ion beam etching of GaAs," *J. Vac. Sci. Technol. B* **8**, 1075-1079.
- Hadley, M.A., Wilson, G.C., Lau, K.Y. and Smith, J.S. (1993) "High single-transverse-mode output from external-cavity surface-emitting laser diodes," *Appl. Phys. Lett.* **63**, 1607-1609.
- Hagberg, M., Jonsson, B. and Larsson, A. (1992) "Fabrication of ultrahigh quality vertical facets in GaAs using pattern corrected electron beam lithography," *J. Vac. Sci. Technol. B* **10**, 2243-2250.
- Hagberg, M., Jonsson, B. and Larsson, A. (1994) "Investigation of chemically assisted ion beam etching for the fabrication of vertical, ultrahigh quality facets in GaAs," *J. Vac. Sci. Technol. B* **12**, 555-566.
- Haney, M.W. (1993) "Self-similar grid patterns in free-space shuffle-exchange networks," *Opt. Lett.* **18**, 2047-2049.

- Hecht, E. and Zajac, A. (1987) *Optics*, (Reading, MA: Addison-Wesley), p. 445-447.
- Horn, M.W., Hartney, M.A. and Kunz, R.R. (1993) "Comparison of etching tools for resist pattern transfer," Opt. Eng. **32**, 2388-2394.
- Juang, Y.Z., Su, Y.K., Shei, S.C. and Fang, B.C. (1994) "Comparing reactive ion etching of III-V compounds in  $\text{Cl}_2/\text{BCl}_3/\text{Ar}$  and  $\text{CCl}_2\text{F}_2/\text{BCl}_3/\text{Ar}$  discharges," J. Vac. Sci. Technol. A **12**, 75-82.
- Koch, B.J., Leger, J.R., Gopinath, A., Wang, Z. and Morgan, R.A. (1997) "Single-mode vertical cavity surface emitting laser by graded-index lens spatial filtering," Appl. Phys. Lett. **70**, 2359-2361.
- Landau, L.D. and Lifshitz, E.M. (1958) *Statistical Physics*, (Reading, MA: Addison-Wesley) p. 455.
- Lee, J.W., Hong, J., Lambers, E.S., Abernathy, C.R., Pearton, S.J., Hobson, W.S. and Ren, F. (1997) "Plasma etching of III-V semiconductors in  $\text{BCl}_3$  chemistries: GaAs and related compounds," Plasma Chemistry and Plasma Processing **17**, 155-167.
- Leger, J.R. and Goltsos, W.C. (1992) "Geometrical transformation of linear diode-laser arrays for longitudinal pumping of solid-state lasers," IEEE J. Quantum Electron. **28**, 1088-1100.
- Leger, J.R., Chen, D. and Dai, K. (1994) "High modal discrimination in a Nd:YAG laser resonator with internal phase gratings," Opt. Lett. **19**, 1976-1978.
- Liang, J.J. and Ballantyne, J.M. (1994) "Self-aligned dry-etching process for waveguide diode ring lasers," J. Vac. Sci. Technol. B **12**, 2929-2932.
- Liau, Z. L. (1991) "Prevention of In evaporation and preservation of smooth surface in thermal annealing and mass transport of InP," Appl. Phys. Lett. **58**, 1869-1871.
- Liau, Z. L. (1996) "Surface vapor transport for accurate microoptics fabrication in compound semiconductors," Mat. Chem. & Phys. **46**, 265-268.
- Liau, Z. L. and Zeiger, H. J. (1990) "Surface-energy-induced mass-transport phenomenon in annealing of etched compound semiconductor structures: theoretical modeling and experimental confirmation," J. Appl. Phys. **67**, 2434-2440.
- Liau, Z.L., Diadiuk, V., Walpole, J.N. and Mull, D.E. (1988) "Large-numerical-aperture InP lenslets by mass transport," Appl. Phys. Lett. **52**, 1859-1861.
- Liau, Z. L., Mull, D. E., Dennis, C. L., Williamson, R. C. and Waarts, R. G. (1994a) "Large-numerical-aperture microlens fabrication by one-step etching and mass-transport smoothing," Appl. Phys. Lett. **64**, 1484-1486.
- Liau, Z. L., Walpole, J. N., Mull, D. E., Dennis, C. L. and Missaggia, L. J. (1994b) "Accurate fabrication of anamorphic microlenses and efficient collimation of tapered unstable-resonator diode lasers," Appl. Phys. Lett. **64**, 3368-3370.
- Liau, Z. L., Mull, D. E. and Hovey, D.L. (1994c) "Fabrication of GaAs microlenses by surface-energy-induced mass transport," *MIT Lincoln Laboratory Quarterly Technical Report: Solid State Research, 9 September 1994*, 1-3.
- Liau, Z. L., Nam, D. W. and Waarts, R. G. (1994d) "Tolerances in microlens fabrication by multilevel etching and mass-transport smoothing," Appl. Opt. **33**, 7371-7376.
- Liau, Z. L., Walpole, J. N., Livas, J. C., Kintzer, E. S., Mull, D. E., Missaggia, L. J. and DiNatale, W. F. (1995)

- "Fabrication of two-sided anamorphic microlenses and direct coupling of tapered high-power diode laser to single-mode fiber," IEEE Photonics Technol. Lett. **7**, 1315-1317.  
1549.
- Morgan, R.A., Guth, G.D., Focht, M.W., Asom, M.T., Kojima, K., Rogers, L.E. and Callis, S.E. (1993) "Transverse mode control of vertical-cavity top-surface-emitting lasers," IEEE Photonics Technol. Lett. **4**, 374-377.
- Morrison, R.L. and Buchholz, D.B. (1998) "Extensible, low-chromatic-sensitivity, all-diffractive-optics relay for interconnecting optoelectronic device arrays," Appl. Opt. **37**, 2925-2934.
- Nikolajeff, F., Hård, S. and Curtis, B. (1997) "Diffractive microlenses replicated in fused silica for excimer laser beam homogenizing," Appl. Opt. **36**, 8481-8489.
- Nikolajeff, F., Ballen, T.A., Leger, J.R., Gopinath, A., Lee, T.-C. and Williams, R.C (1999) "Spatial-mode control of vertical-cavity lasers with micromirrors fabricated and replicated in semiconductor materials," Appl. Opt. **38**, 3030-3038.
- Sankur, H., Hall, R., Motamedi, E., Gunning, W. and Tennant, W. (1996) "Fabrication of microlens arrays by reactive ion milling," Proc. SPIE **2687**, 150-155.
- Shewmon, P. (1989) *Diffusion in Solids*, (Warrendale, PA: The Minerals, Metals & Materials Society), Chapter 1.
- Sinzinger, S. and Jahns, J. (1997) "Integrated micro-optical imaging system with a high interconnection capacity fabricated in planar optics," Appl. Opt. **36**, 4729-4735.
- Stern, M.B. and Medeiros, S.S. (1992) "Deep three-dimensional microstructure fabrication for infrared binary optics," J. Vac. Sci. Technol. B **10**, 2520-2525.
- Swanson, G.J. (1989) "Binary Optics Technology: The Theory and Design of Multi-Level Diffractive Optical Elements," *MIT Lincoln Laboratory Technical Report 854*.
- Swenson, J.S., Fields, R.A. and Abraham, M.H. (1995) "Enhanced mass-transport smoothing of f/0.7 GaP microlenses by use of sealed ampoules," Appl. Phys. Lett. **66**, 1304-1306.
- Tiberio, R. C., Porkolab, G. A., Johnson, J. E., Grande, W. J., Rathbun, L.C., Wolf, E. D., Craighead, H. G., Lang, R. J., Larsson, A., Forouhar, S. and Cody, J. (1990) "Electron-beam lithography and chemically assisted ion beam etching for the fabrication of grating surface-emitting broad-area AlGaAs lasers," J. Vac. Sci. Technol. B **8**, 1408-1411.
- Tooley, F.A.P. (1996) "Challenges in optically interconnecting electronics," IEEE J. Selected Topics in Quant. Electron. **2**, 3-13.
- Wendt, J.R., Vawter, G.A., Smith, R.E. and Warren, M.E. (1995) "Nanofabrication of subwavelength, binary, high-efficiency diffractive optical elements in GaAs," J. Vac. Sci. Techn. B **13**, 2705-270.
- Wilson, G.C., Hadley, M.A., Smith, J.S. and Lau, K.Y. (1993) "High single-mode output power from external microcavity surface-emitting laser diode," Appl. Phys. Lett. **63**, 3265-3267.
- Youtsey, C., Grundbacher, R., Panepucci, R., Adesida, I. and Caneau, C. (1994) "Characterization of chemically assisted ion beam etching of InP," J. Vac. Sci. Technol. B **12**, 3317-3321.